Baroclinic Vortices in Rotating Stratified Shearing Flows: Cyclones, Anticyclones, and Zombie Vortices

by

Pedram Hassanzadeh

A dissertation submitted in partial satisfaction of the
requirements for the degree of
Doctor of Philosophy

in

Engineering – Mechanical Engineering

in the

Graduate Division

of the

University of California, Berkeley

Committee in charge:

Professor Philip S. Marcus, Chair
Professor Tarek I. Zohdi
Professor Edgar Knobloch

Spring 2013

Baroclinic Vortices in Rotating Stratified Shearing Flows: Cyclones, Anticyclones, and Zombie Vortices

Abstract

Baroclinic Vortices in Rotating Stratified Shearing Flows: Cyclones, Anticyclones, and Zombie Vortices

by

Pedram Hassanzadeh

Doctor of Philosophy in Engineering – Mechanical Engineering

University of California, Berkeley

Professor Philip S. Marcus, Chair

Large coherent vortices are abundant in geophysical and astrophysical flows. They play significant roles in the Earth's oceans and atmosphere, the atmosphere of gas giants, such as Jupiter, and the protoplanetary disks around forming stars. These vortices are essentially three–dimensional (3D) and baroclinic, and their dynamics are strongly influenced by the rotation and density stratification of their environments. This work focuses on improving our understanding of the physics of 3D baroclinic vortices in rotating and continuously stratified flows using 3D spectral simulations of the Boussinesq equations, as well as simplified mathematical models. The first chapter discusses the big picture and summarizes the results of this work.

In Chapter 2, we derive a relationship for the aspect ratio (i.e., vertical half–thickness over horizontal length scale) of steady and slowly–evolving baroclinic vortices in rotating stratified fluids. We show that the aspect ratio is a function of the Brunt-Väisälä frequencies within the vortex and outside the vortex, the Coriolis parameter, and the Rossby number of the vortex. This equation is basically the gradient–wind equation integrated over the vortex, and is significantly different from the previously proposed scaling laws that find the aspect ratio to be only a function of the properties of the background flow, and independent of the dynamics of the vortex. Our relation is valid for cyclones and anticyclones in either the cyclostrophic or geostrophic regimes; it works with vortices in Boussinesq fluids or ideal gases, and non–uniform background density gradient. The relation for the aspect ratio has many consequences for quasi–equilibrium vortices in rotating stratified flows. For example, cyclones must have interiors more stratified than the background flow (i.e., super–stratified), and weak anticyclones must have interiors less stratified than the background (i.e., sub–stratified). In addition, this equation is useful to infer the height and internal stratification of some astrophysical and geophysical vortices because direct measurements of their vertical structures are difficult. We verify our relation for the aspect ratio with numerical simulations for a wide variety of families of vortices, including: vortices that are initially in (dissipationless) equilibrium and then evolve due to an imposed weak viscous dissipation

or density radiation; anticyclones created by the geostrophic adjustment of a patch of locally mixed density; cyclones created by fluid suction from a small localized region; vortices created from the remnants of the violent breakups of columnar vortices; and weakly non-axisymmetric vortices. The values of the aspect ratios of our numerically–computed vortices validate our theoretically–derived relationship for aspect ratio, and generally they differ significantly from the values obtained from the much–cited conjecture that the aspect ratio of quasi-geostrophic vortices is equal to the ratio of the Coriolis parameter to the Brunt-Väisälä frequency of the background flow.

In Chapter 3, we show numerically and experimentally that localized suction in rotating continuously stratified flows produces three–dimensional baroclinic cyclones. As expected from Chapter 2, the interiors of these cyclones are super–stratified. Suction, modeled as a small spherical sink in the simulations, creates an anisotropic flow toward the sink with directional dependence changing with the ratio of the Coriolis parameter to the Brunt-Väisälä frequency. Around the sink, this flow generates cyclonic vorticity and deflects isopycnals so that the interior of the cyclone becomes super-stratified. The super–stratified region is visualized in the companion experiments that we helped to design and analyze using the synthetic schlieren technique. Once the suction stops, the cyclones decay due to viscous dissipation in the simulations and experiments. The numerical results show that the vertical velocity of viscously decaying cyclones flows away from the cyclone's midplane, while the radial velocity flows toward the cyclone's center. This observation is explained based on the cyclo–geostrophic balance. This vertical velocity mixes the flow inside and outside of cyclone and reduces the super–stratification. We speculate that the predominance of anticyclones in geophysical and astrophysical flows is due to the fact that anticyclones require sub–stratification, which occurs naturally by mixing, while cyclones require super–stratification.

In Chapter 4, we show that a previously unknown instability creates space–filling lattices of 3D turbulent baroclinic vortices in linearly–stable, rotating, stratified shear flows. The instability starts from a newly discovered family of easily–excited critical layers. This new family, named the baroclinic critical layer, has singular vertical velocities; the traditional family of (barotropic) critical layer has singular stream–wise velocities and is hard to excite. In our simulations, the baroclinic critical layers in rotating stably–stratified linear shear are excited by small–volume, small–amplitude vortices or waves. The excited baroclinic critical layers then intensify by drawing energy from the background shear and roll–up into large coherent 3D vortices that excite new critical layers and vortices. The vortices self–similarly replicate to create lattices of turbulent vortices. These vortices persist for all time and are called zombie vortices because they can occur in the dead zones of protoplanetary disks. The self–replication of zombie vortices can de-stabilize the otherwise linearly and finite–amplitude stable Keplerian shear and lead to the formation of stars and planets.

Everything should be made as simple as possible, but not simpler
A. Einstein

Contents

Acknowledgments

It was the best of times, it was the age of wisdom, it was the epoch of belief, it was the season of Light, it was the spring of hope, I had everything before me; these words well describe my five years in UC Berkeley as a Ph.D. student. I owe this great time to a group of amazing people and here is a chance to thank some of them.

First and foremost, I would like to thank my Ph.D. advisor Philip Marcus. Phil's passion, devotion, depth and breadth of knowledge, energy, integrity, and kindness the most perfect Ph.D. advisor I could have dreamed of. He patiently taught me fluid dynamics, math, computation, and geophysical fluid dynamics; he also showed me how to approach a new problem, how to simplify it, and how not to oversimplify it. I am grateful to Phil for thoughtfully mentoring me through the first two years of my Ph.D., and then giving me more freedom and flexibly while providing invaluable input, guidance, and criticism. Not far into my Ph.D., I started to think of Phil as not only my advisor but also as a friend (the smarter, more experienced kind of friend everybody looks for), and I would like to thank him for all of his advice and support. Thank you Phil for this wonderful and rewarding journey.

I am very grateful to my labmate Chung-Hsiang Jiang for what he has patiently taught me, for his help with computation, and for his great advice about research, coursework, career, etc. I would like to deeply thank another labmate, Suyang Pei, for our wonderful collaboration over the past five years; I learned so much from Suyang, and he has been always extremely generous in sharing his ideas and results, and very patient with explaining them to me. Working with Chung-Hsiang and Suyang made my Ph.D. way more fruitful and enjoyable. I would like to express my gratitude toward Oriane Aubert, Patrice Le Gal, and Michael Le Bars in IRPHE for our productive and stimulating collaboration. Furthermore, I am very grateful to Patrice for teaching me a lot about waves, instabilities, vortices, and experiments; for his kind support in various occasions; and for showing me how a scientific collaboration can be fun as well. I would like to thank Oriane for our numerous Skype conversations about vortices and rotating stratified flows. I appreciate Michael's support, and his feedback and contribution to this work.

I would like to thank Ömer Savas for teaching me fluid mechanics, for his advice and support throughout the years, and for chairing my qualifying exam. Much appreciation goes to the members of my qualifying exam and dissertation committees: Tarek Zohdi, Per Persson, David Steigmann, and Edgar Knobloch. In particular, I am grateful to Edgar for his comments on my dissertation, for his support, and for his wonderful course on dynamical systems, which showed me how much math I do not know. I truly enjoyed and benefited from the well-taught courses that I took in UC Berkeley. In addition to Phil, Ömer, Edgar, David, and Per, I would like to thank Panos Papadopoulos, John Neu, James Sethian, Alexandre Chorin, Grigory Barenblatt, and Van Carey.

I spent the summer of 2012 as a GFD Fellow at the Woods Hole Oceanographic Institution where I worked with Charlie Doering and Greg Chini. They insightfully guided me through the well-designed and exciting project, and I sincerely appreciate their devotion and support. I would like to thank all the fellows and participants of the GFD program, in particular

George Veronis, for this wonderful experience. I would like to thank Jon Wilkening for a careful review of this work, which was turned into a master's thesis in mathematics. In Woods Hole, I greatly enjoyed and benefited from the lectures by Jeff Weiss on vortices and coherent structures. He clarified many subtle key points for me.

I would like to thank the current and former members of our lab: Joe Barranco, Sushil Shetty, Xylar Asay–Davis, Meng Wang, Caleb Levy, Mani Mahdinia, Sahuck Oh, and Omid Solari. In particular, I am grateful to Joe for developing the parallel spectral code which became the basis of my code, to Sushil for helpful suggestions and encouragement at the beginning of my Ph.D., and to Caleb for his help with running and post-processing some of the simulations. I would like to thank Caleb and Kenneth Lee for carefully proofreading parts of this dissertation. I appreciate scholarships form the Natural Sciences and Engineering Research Council of Canada, the Woods Hole Oceanographic Institution, and the Jonathan Laitone Memorial Scholarship Fund. I would also like to thank the staff in Brewed Awakening, especially P. J. and Eric, for their good coffee and friendly chitchat.

I am very grateful to George Raithby, my master's thesis advisor in the University of Waterloo, for accepting me as his student, for teaching me computation and heat transfer, and above all, for helping me to mature and transform from an undergraduate student to a graduate student and researcher. George (along with my friend Amir Baserinia) also helped me to adapt to the culture and environment, and he gently forced me to improve my English (which I did by watching each episode of Seinfeld 10 times). I would also like to thank Gordon Stubley and Metin Renksizbulut for the well–taught courses and for their support.

I would like to thank Vahid Esfahanian who introduced me to the amazing world of fluid dynamics and computation in my sophomore year. He then hired me in his lab and provided me a great opportunity to do research and acquire valuable skills. I have been using what I learned from Vahid almost every day in grad school. Furthermore, I am grateful to Farschad Torabi and Ahmad Javaheri (famil) for being great teachers, supporters, and friends. As an undergrad, I learned so much from courses offered by Mehrdad Raisee and Mehdi Ashjaee. I would also like to thank Mehrdad for his support, and for encouraging me to study abroad.

I have been blessed with great friends in my life, and they have generously shared their thoughts, time, knowledge, and happiness with me. Some of these friends have had a deep impact on my life and have made me a much better and happier person. Thank you Sara Toutiaei, Ashkan Borna, Arman Hajati, Arash Tajik, Azad Zade, Saba Pasha, Kenny Lee, Sobhan Seyfaddini, Farzaneh Shahrokhi, Donna Artusy, Alireza Lahijanian, Heather Kittel, Nader Norouzi, Mehdi Dargahi, Sahar Tabesh, Amin Arbabian, Azadeh Bozorgzadeh, Benjamin Jarrahi, Nasim Alem, Jay Keist, Arash Raisee, Farzad Houshmand, Meysam Rezaee, Mohsen Shahini, Laleh Davis, Mehrzad Tartibi, Caroline Uhler, Debanjan Mukherjee, Bahador Jafarpur, Sunny Mistry, Giorgio de Vera ...

Above all, I am indebted to my great family, my parents Safa and Hossein and my sister Pegah, for their endless and selfless love, encouragement, and support. Words cannot describe my love for them, and my gratitude for what they have done for me.

Chapter 1

Geophysical and Astrophysical Vortices

Large coherent vortices are abundant in geophysical and astrophysical flows. These persistent vortices, which are tens to millions of kilometers in diameter, strongly interact with their environment. For example, vortices of the Agulhas Current (Figure 1.1) and Mediterranean eddies, called Meddies, (Figure 1.2) carry warm water into the Atlantic ocean and transport a huge amount of salinity, nutrients, and chemicals for large distances [Armi et al., 1988, Klein and Lapeyre, 2009]. Tropical cyclones [Rossby, 1949] and polar vortices [McIntyre, 1995] are examples of vortices in the Earth's atmosphere; the latter play an important role in the stratospheric dynamics and have contributed to the ozone depletion [McIntyre, 1989, Waugh and Polvani, 2010]. Studying the physics of geophysical vortices and their impact on the oceanic and atmospheric circulations, climate, and the ecosystem is an active area of research. However, the difficulties of in–situ measurements and well–resolved simulations of large–scale flows pose a big challenge to these studies [Siegel et al., 2001, Khouider et al., 2013, Ghil et al., 2008].

Atmospheres of the gas giants are also filled with large long–lived vortices. Examples are Jupiter's Great Red Spot [Hooke, 1665] and Oval BA [Go et al., 2006] (Figure 1.3), Saturn's polar vortices [Godfrey, 1988, Sánchez-Lavega et al., 2006] and Neptune's Great Dark Spot [Smith et al., 1989]. These vortices cause significant mixing and transport of heat across these planets and their disappearance might lead to a global climate change [Marcus, 2004]. Although some of these vortices, such as the Great Red Spot, have been extensively studied, many questions about their color and color–change [Wong et al., 2011, Marcus et al., 2013a], longevity [Ingersoll and Cuong, 1981, Vasavada and Showman, 2005, Sommeria et al., 1988], vertical and horizontal structures [de Pater et al., 2010, Fletcher et al., 2010, Morales-Juberías and Dowling, 2013], and interaction with the zonal flows [Salyk et al., 2006, Shetty et al., 2007, Marcus, 1988] are still not answered.

Vortices exist even beyond our solar system. It has been speculated [Abramowicz et al., 1992] that coherent vortices play an important role in the formation of stars [McKee and Ostriker, 2007] and planets [Lissauer, 1993] in the protoplanetary disks. This is because

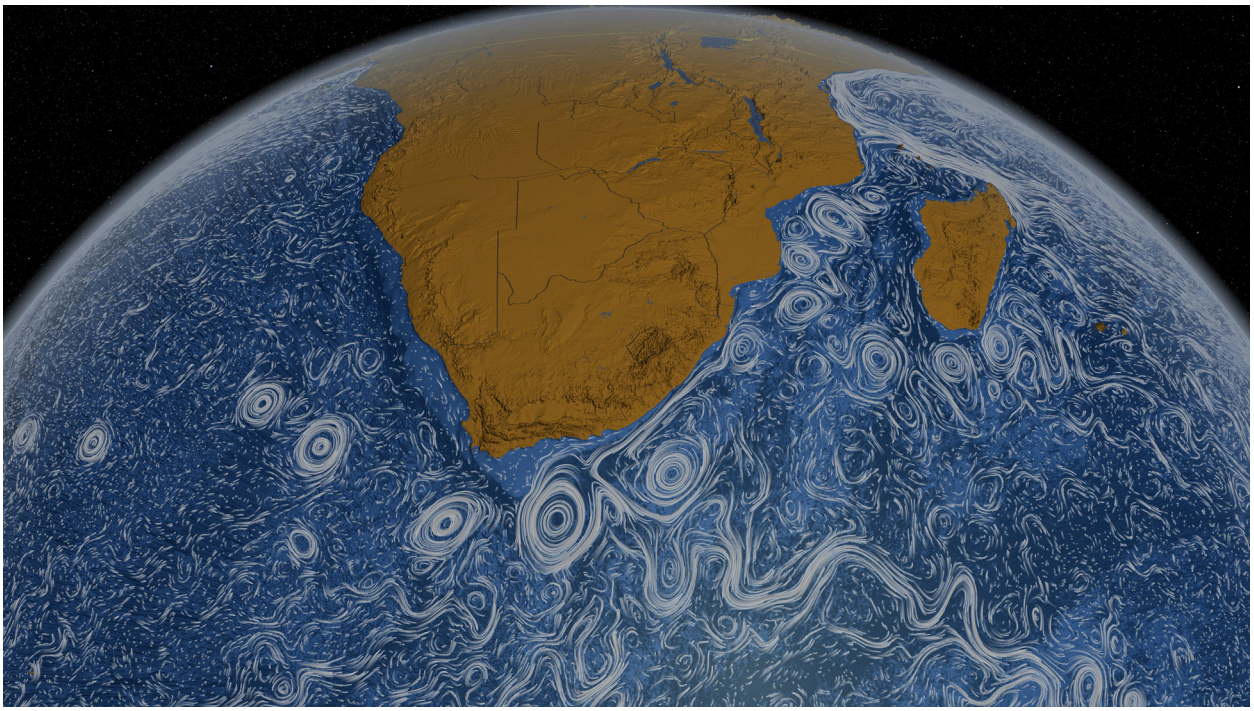

Figure 1.1: Vortices at the surface of the Agulhas Current off the African coast. See http://svs.gsfc.nasa.gov/vis/a000000/a003800/a003827/ for details and a movie of the Earth's surface currents (Credit: NASA/Goddard Space Flight Center Scientific Visualization Studio).

vortices can efficiently transport angular momentum and possibly de–stabilize the Keplerian shear [Barranco and Marcus, 2005, Lyra and Mac Low, 2012] in the regions that the magneto–rotational instability cannot operate (i.e., the dead zones) [Balbus and Hawley, 1998]. Furthermore, anticyclonic vortices can accumulate dust in their cores and form planetesimals [Barge and Sommeria, 1995, Bracco et al., 1999, Klahr and Bodenheimer, 2006]. However, the formation and stability of baroclinic vortices in compressible Keplerian shear are not fully understood [Armitage, 2011, Barranco and Marcus, 2005].

Geophysical and astrophysical vortices, a few listed above, have various length and time scales and exist in very different environments. However, what is common among them is that their physics are strongly influenced by the background rotation and density stratification. Therefore, as an alternative to studying specific geophysical and astrophysical vortices, one might propose a generic study of vortices in rotating stratified flows to answer some of the common questions about them:

- Creation: what are the mechanisms creating vortices, and how do the vortices generated with various mechanisms differ?
- Decay: how do the vortices evolve and decay subjected to dissipating processes such

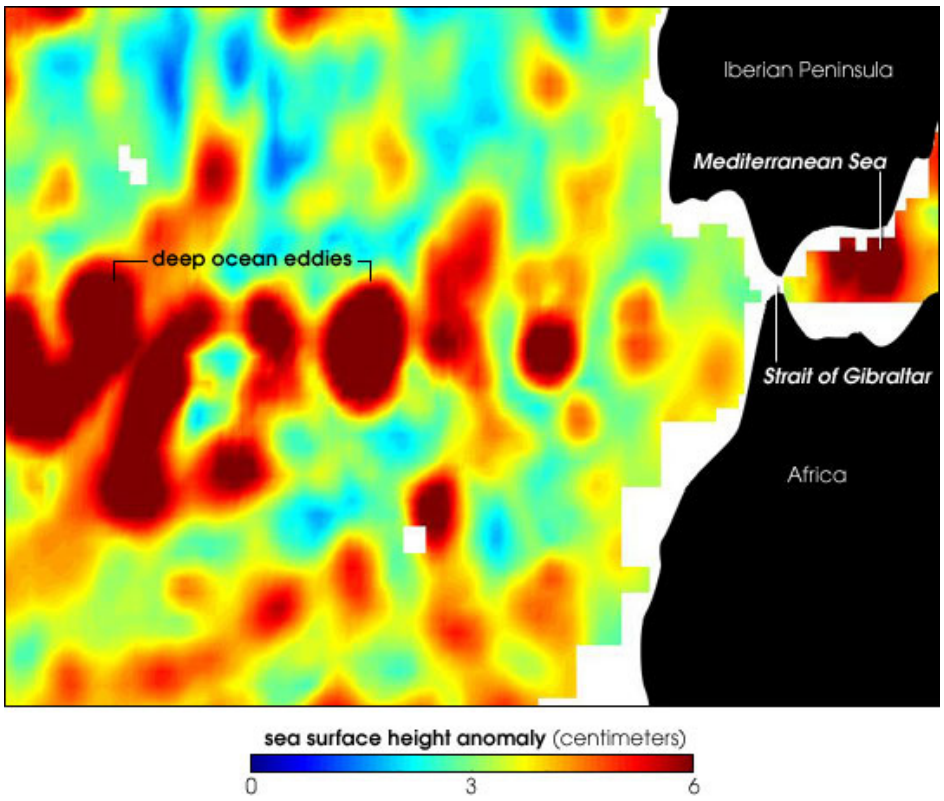

Figure 1.2: Anticyclonic Meddies, form 1 km deep in the Atlantic Ocean, visualized using satellite sea–surface height measurements. Surface signature of anticyclones is elevation in the sea–surface height, which is shown in red (Credit: University of Delaware).

as eddy viscosity and thermal radiation?

- Longevity: what are the mechanisms that can force and maintain a vortex against dissipating mechanisms?
- Secondary circulation[1]: what is the role of the usually weak meridional secondary flow?
- Size: what sets the vertical and horizontal length scales of vortices?
- Asymmetry: how do the dynamics of cyclones and anticyclones differ?
- Stability: what are the linear and finite–amplitude stability properties as a function of the parameters of the vortex and the background flow?

[1]The secondary circulation discussed here is different from Ekman pumping, see Section 3.6.

Figure 1.3: The Great Red Spot (right) and Oval BA (left) are two gigantic anticyclones in the Southern Hemisphere of Jupiter. The picture is taken by the Hubble Space Telescope (Credit: NASA).

- Interaction: how do vortices interact with each other (e.g., merge), and with the mean flow and waves? An important subset of this question is the mixing and stirring the vortices induce in their surrounding.

This list is far from complete and these are just some of the questions encountered in the course of this work. As discussed briefly below and in detail in the next chapters, the answers to some of these questions are intertwined. The purpose of this study is to improve our understanding of baroclinic vortices in rotating stratified flows using high–resolution three-dimensional numerical simulations of the non–hydrostatic Boussinesq equations and simplified mathematical models.

In Chapter 2, which appears in Hassanzadeh et al. [2012], a new equation is derived and numerically validated that relates the aspect ratio (i.e., ratio of the vertical to horizontal length scales) of vortices in quasi–equilibrium to their Rossby number and internal stratification, and the Coriolis parameter and stratification of the background flow. The new equation is essentially the gradient–wind equation [Vallis, 2006] integrated over the vortex, and can be used to infer the vertical structure of vortices from observational data, as well as to develop simplified models for baroclinic vortices (e.g., to model mixing or for parametrization in the global circulation models). This equation significantly differs from the previously proposed scaling laws for the aspect ratio, which are shown to be inconsistent with the gradient–wind equation and our numerical results. These results give a new insight into the dynamics of

the baroclinic vortices and in particular the role of the secondary circulation. The simulations show that the interior stratifications of a vortex evolves in time and space because of a meridional secondary circulation induced by weak dissipating processes. The weak secondary circulation is also found to affect the time evolution of the velocity field of the vortex and change the Rossby number.

In ongoing work not presented in this dissertation, numerical results show that the decay of dissipating vortices, in particular in the presence of zonal shear, can be significantly slowed down by the secondary circulation because of its capability to efficiently convert the kinetic energy to potential energy and vice versa (preliminary results are presented in Marcus and Hassanzadeh [2011] and Hassanzadeh and Marcus [2012]). These results might explain the unexpected longevity[2] of some of the oceanic [Armi et al., 1989] and planetary vortices [Ingersoll, 1990] with no need of a strong forcing mechanism. Note that most numerical studies in the past have used hydrostatic or two–dimensional models resulting in the secondary circulation being either absent or not accurately represented.

Chapter 3, which appears in Hassanzadeh et al. [2013], discusses one of the mechanisms to produce baroclinic vortices in nature and in laboratory: localized suction. Numerical simulations and laboratory experiments show that a baroclinic cyclone with an interior more stratified than the background flow (i.e., super–stratified) is produced as a result of suction. The fact that the cyclones have super–stratified interiors, as opposed to anticyclones which have less stratified interiors, can be a major contributor to the cyclone–anticyclone asymmetry in rotating stratified turbulence. The role of the secondary circulation in mixing the inside and outside of the cyclone and reducing the super–stratification once the suction stops is also studied.

Chapter 4, which appears in Marcus et al. [2013b], presents a new family of critical layers for rotating stably–stratified shear that has singularity in vertical velocities[3]. High–resolution three–dimensional simulations show that baroclinic critical layers are easily exited by a single small–volume vortex, form stripes of strong vertical vorticity, and subsequently roll up and produce new vortices, which in turn excite new layers. The vortices self–replicate and populate the entire computational domain. This instability is expected to be ubiquitous in the dead zones of the protoplanetary disks. Such purely hydrodynamic instability in the dead zones has been long searched for in simulations and experiments without success [Balbus and Hawley, 1998, Ji et al., 2006, Paoletti et al., 2012]. We believe that the baroclinic critical layers and their instability have not been observed previously because of one or more of the following in the past studies: focusing on constant–density fluids in most experiments and some simulations; small apparatuses and parameter–regime in some experiments; lack of resolution, using hydrostatic models, unphysical initial conditions, and performing two–dimensional simulations in many of the computational studies.

[2]For example, the Great Red Spot has survived for over 300 years despite having a radiative time scale of ≈ 10 years [Marcus, 1993].

[3]See Boulanger et al. [2007] for an analytical and experimental analysis of a similar but not quite the same family of critical layers.

Apart from improving our answers to some of the questions asked before (e.g., aspect ratio and vertical structure, creation, secondary circulation, etc.), this work demonstrates that important aspects of the physics of geophysical and astrophysical flows may be missed in two–dimensional or hydrostatic simulations, or in studies that ignore the vertical stratification; hence "everything should be made as simple as possible, but not simpler".

Chapter 2

Universal Aspect Ratio of Baroclinic Vortices

2.1 Introduction

Compact three–dimensional baroclinic vortices are abundant in geo- and astrophysical flows. Examples in planetary atmospheres include the rows of cyclones and anticyclones near Saturn's *Ribbon* [Sayanagi et al., 2010] and near 41°S on Jupiter [Humphreys and Marcus, 2007], and Jupiter's anticyclonic Great Red Spot [Marcus, 1993]. In the Atlantic ocean, meddies persist for years [Armi et al., 1988, McWilliams, 1985], and numerical simulations of the disks around protostars produce compact anticyclones [Barranco and Marcus, 2005]. The physics that create, control, and decay these vortices are highly diverse, and the aspect ratios $\alpha \equiv H/L$ of these vortices range from flat "pancakes" to nearly round (where H is the vertical half-height and L is the horizontal length scale of the vortex). However, we shall show that the aspect ratios of the vortices all obey a universal relationship.

Our relation for α differs from previously published ones, including the often-used $\alpha = f/\bar{N}$, where f is the Coriolis parameter, $N \equiv \sqrt{-\frac{g}{\rho}\frac{\partial \rho}{\partial z}}$ is the Brunt-Väisälä frequency, g is the acceleration of gravity, z is the vertical coordinate, ρ is the density for Boussinesq flows and potential density for compressible flows; and a bar over a quantity indicates that it is the value of the unperturbed (i.e., with no vortices) background flow. We shall show that $\alpha = f/\bar{N}$ is not only incorrect by factors of 10 or more in some cases, but also that it is misleading; it suggests that α depends only on the background flow and not on the properties of the vortex, so that *all* vortices embedded in the same flow (e.g., in the Atlantic or in the Jovian atmosphere) have the same α. We shall show that this is *not* true. Knowledge of the

With minor modifications, Chapter 1 is reprinted with permission from:
P. Hassanzadeh, P. S. Marcus, and P. Le Gal, *The Universal Aspect Ratio of Vortices in Rotating Stratified Flows: Theory and Simulation*, Journal of Fluid Mechanics, (706), 2012.

correct relation for α is important. For example, there has been debate over whether the color change, from white to red, of Jupiter's anticyclone Oval BA, was due to a change in its H [de Pater et al., 2010]. Measurements of the half-heights H of planetary vortices are difficult, but H could be accurately inferred if the correct relation for α were known. We validate our relation for α with 3D numerical simulations of the Boussinesq equations. A companion paper by [Aubert et al., 2012] validates it with laboratory experiments and with observations of Atlantic ocean meddies and Jovian vortices.

2.2 Aspect Ratio: Derivation

We assume that the rotation axis and gravity are parallel and anti-parallel to the vertical z axis, respectively. We also assume that the vortices are in approximate cyclo-geostrophic balance horizontally and hydrostatic balance vertically (referred to hereafter as CG-H balance). Necessary approximations for CG-H balance are that the vertical v_z and radial v_r velocities are negligible compared to the azimuthal one v_θ (where the origin of the cylindrical coordinate system is at the vortex center), that dissipation is negligible, and that the flow is approximately steady in time. With these approximations, the radial r and azimuthal θ components of Euler's equation in a rotating frame are

$$\frac{\partial p}{\partial r} = \rho v_\theta \left(f + \frac{v_\theta}{r} \right) \tag{2.1}$$

$$\frac{\partial p}{\partial z} = -\rho g, \tag{2.2}$$

where p is the pressure. We have assumed that the vortex is axisymmetric, but we show later numerically in Section 2.7 that this approximation can be relaxed. Following the convention, we ignored the centrifugal term $\rho f^2 r/4 \, \hat{\mathbf{r}}$ in equation (2.1) by assuming that the centrifugal buoyancy is much smaller than the gravitational buoyancy, i.e. that the rotational Froude number $f^2 d/(4g) \ll 1$, where d is the characteristic distance of the vortex from the rotation axis [see e.g. Barcilon and Pedlosky, 1967]. The θ-component of Euler's equation, continuity equation, and the equation governing the dissipationless transport of (potential) density are all satisfied by a steady, axisymmetric flow with $v_r = v_z = 0$. As a consequence, equations (2.1) and (2.2) are the only equations that need to be satisfied for both Boussinesq and compressible flows. Thus, our relation for α will also be valid for both of these flows. Far from the vortex, where $\mathbf{v} = 0$, $p = \bar{p}$, and $\rho = \bar{\rho}$, (2.1) and (2.2) reduce to

$$\frac{\partial \bar{p}}{\partial r} = 0 \tag{2.3}$$

$$\frac{\partial \bar{p}}{\partial z} = -\bar{\rho} g \tag{2.4}$$

showing that $\bar{p}$ and $\bar{\rho}$ are only functions of z. Subtracting equations (2.3) and (2.4) from (2.1) and (2.2):

$$\frac{\partial \tilde{p}}{\partial r} = \rho v_\theta \left(f + \frac{v_\theta}{r} \right) \tag{2.5}$$

$$\frac{\partial \tilde{p}}{\partial z} = -\tilde{\rho} g \tag{2.6}$$

where $\tilde{p} \equiv p - \bar{p}$ and $\tilde{\rho} \equiv \rho - \bar{\rho}$ are respectively the pressure and density anomalies. The center of a vortex ($r = z = 0$) is defined as the location on the z-axis where $\tilde{p}$ has its extremum, so equation (2.6) shows that at the vortex center (denoted by a c subscript) $\tilde{\rho}_c = 0$ or $\rho_c = \bar{\rho}(0) \equiv \rho_o$. At the vortex boundary and outside the vortex, where v_θ and $\tilde{\rho}$ are negligible, equations (2.5) and (2.6) show that $\tilde{p} \simeq 0$.

We define the pressure anomaly's characteristic horizontal length scale (i.e. radius) as

$$L \equiv \sqrt{\left| \frac{4\tilde{p}_c}{(\nabla_\perp^2 \tilde{p})_c} \right|}, \tag{2.7}$$

where the subscript $\perp$ means *horizontal component*. Integrating (2.5) from the vortex center to its side boundary at $(r, z) = (L, 0)$ approximately yields

$$-\frac{\tilde{p}_c}{L} = \rho_o V_\theta \left(f + \frac{V_\theta}{R_v} \right) \tag{2.8}$$

where in the course of integration, ρ has been replaced with ρ_o, which is exact for Boussinesq flows, and an approximation for fully compressible flows. Here V_θ is the characteristic peak azimuthal velocity, and R_v is the approximate radius where the velocity has that peak. The analytical and numerically simulated vortices discussed below, meddies, and the laboratory vortices examined by [Aubert et al., 2012] all have $R_v \approx L$, but *hollow* vortices with quiescent interiors have $R_v \neq L$. For example, the Great Red Spot has $R_v \simeq 3L$ [Shetty and Marcus, 2010]. Similarly, integrating (2.6) from the vortex center to its top boundary at $(r, z) = (0, H)$ approximately gives

$$\frac{\tilde{p}_c}{H} = g\tilde{\rho}(r = 0, z = H), \tag{2.9}$$

where H is the pressure anomaly's characteristic vertical length scale (i.e. half-height),

$$H \equiv \sqrt{\left| \frac{2\tilde{p}_c}{(\partial^2 \tilde{p}/\partial z^2)_c} \right|}. \tag{2.10}$$

Equations (2.8) and (2.9) can be combined to eliminate $\tilde{p}_c$:

$$\frac{\rho_o V_\theta (f + V_\theta/R_v)}{H} = -\frac{g\tilde{\rho}(r = 0, z = H)}{L}. \tag{2.11}$$

Notice that this equation is basically the *thermal wind* equation, with the cyclostrophic term included (i.e. the gradient-wind equation [Vallis, 2006]), integrated over the vortex. Using the first term of a Taylor series, we approximate $\tilde{\rho}(r = 0, z = H)$ on the right-hand side of (2.11) with

$$\begin{aligned} \tilde{\rho}(r = 0, z = H) &= \tilde{\rho}_c + H(\partial\tilde{\rho}/\partial z)_c \\ &= H[(\partial\rho/\partial z)_c - (\partial\bar{\rho}/\partial z)_c] \\ &= \rho_o H(\bar{N}^2 - N_c^2)/g \end{aligned} \tag{2.12}$$

where $\tilde{\rho} \equiv \rho - \bar{\rho}$ and $\tilde{\rho}_c = 0$ have been used. Note that in general, $\bar{N}(z)$ is a function of z; however, the only way in which $\bar{N}(z)$ is used in this derivation (or anywhere else in this paper) is at $z = 0$ for evaluating $(\partial\bar{\rho}/\partial z)_c$. Therefore, rather than using the cumbersome notation $\bar{N}_c$, we simply use $\bar{N}$.

Using (2.12) in equation (2.11) gives our relation for α:

$$\alpha^2 \equiv \left(\frac{H}{L}\right)^2 = \frac{Ro\ [1 + (L/R_v)\, Ro]}{N_c^2 - \bar{N}^2} f^2 \tag{2.13}$$

where the Rossby number defined as $Ro \equiv V_\theta/(fL)$ can be well approximated as

$$Ro = \omega_c/(2f), \tag{2.14}$$

ω_c being the vertical component of vorticity at the vortex center. Defining the Burger number as

$$Bu \equiv \left(\frac{\bar{N}H}{fL}\right)^2, \tag{2.15}$$

equation (2.13) may be as well rewritten as

$$\left[\left(\frac{N_c}{\bar{N}}\right)^2 - 1\right] Bu = Ro\ \left[1 + \frac{L}{R_v} Ro\right] \tag{2.16}$$

Equation (2.13) shows that α depends on two properties of the vortex: Ro and the *difference* between the Brunt-Väisälä frequencies inside the vortex (i.e. N_c^2) and outside the vortex (i.e. $\bar{N}^2$). Note that to derive relation (2.13), no assumption has been made on the compressibility of the flow, Rossby number smallness, dependence of $\bar{N}$ on z, or the magnitude of $N_c/\bar{N}$. Therefore, equation (2.13) is applicable to Boussinesq, anelastic [Vallis, 2006], and fully compressible flows, cyclones (i.e., $Ro > 0$) and anticyclones (i.e., $Ro < 0$), and geostrophic and cyclostrophic flows. In the cyclostrophic limit (i.e., $|Ro| \gg 1$) with $N_c = 0$ and $R_v = L$,

$$Ro\,(1 + Ro) \to Ro^2, \tag{2.17}$$

hence equation (2.13) becomes $V_\theta = H\bar{N}$, agreeing with the findings of [Billant and Chomaz, 2001] and others. Equation (2.13) is easily modified for use with discrete layers of fluid rather than a continuous stratification, and in that case agrees with the work of [Nof, 1981] and [Carton, 2001].

Equation (2.13) has several consequences for equilibrium vortices. For example, because the right-hand side of (2.13) must be positive, cyclones must have $N_c^2 \geq \bar{N}^2$. Another consequence is that anticyclones with $-Ro < R_v/L$, must have $N_c^2 \leq \bar{N}^2$, and anticyclones with $-Ro > R_v/L$, have $N_c^2 \geq \bar{N}^2$. In addition, equation (2.13) is useful for astrophysical and geophysical observations of vortices in which some of the vortex properties are difficult to measure. For example, N_c is difficult to measure in some ocean vortices [Aubert et al., 2012], and H is difficult to determine in some satellite observations of atmospheric vortices [de Pater et al., 2010], but their values can be inferred from equation (2.13).

Note that N_c is a measure of the mixing within the vortex; if the density is not mixed with respect to the background flow, then $N_c \to \bar{N}$ (and the vortex is a tall, barotropic Taylor column); if the density is well-mixed within the vortex so the (potential) density is uniform inside the vortex, then $N_c \to 0$ (as in the experiments of [Aubert et al., 2012]); if $N_c^2 > \bar{N}^2$ (as required by cyclones), then the vortex is more stratified than the background flow.

2.3 Previously Proposed Scaling Laws

Other relations for α that differ from our equation (2.13) have been published previously, and the most frequently cited one is

$$\alpha \equiv \frac{H}{L} = \frac{f}{\bar{N}}. \tag{2.18}$$

This relationship is inferred from Charney's equation for the quasi-geostrophic (QG) potential vorticity [equation (8) in Charney, 1971] that was derived for flows with $|Ro| \ll 1$ and $N_c/\bar{N} \simeq 1$. Separately re-scaling the vertical and horizontal coordinates of the potential vorticity equation, and then assuming that the vortices are isotropic in the re-scaled (but not physical) coordinates, one obtains the alternative scaling $\alpha = f/\bar{N}$. Numerical simulations of the QG equation for some initial conditions have produced turbulent vortices with $H/L \approx f/\bar{N}$ [c.f., McWilliams et al., 1999, Dritschel et al., 1999, Reinaud et al., 2003], even though significant anisotropy in the re-scaled coordinates was observed in similar simulations [McWilliams et al., 1994]. The constraints under which the QG equation is derived are very restrictive; for example, none of meddies or laboratory vortices studied by [Aubert et al., 2012] meet these requirements because $N_c/\bar{N}$ is far from unity. Therefore, it is not surprising that none of these vortices, including the laboratory vortices, agree with $\alpha \approx f/\bar{N}$, but instead have α in accord with relation (2.13) [Aubert et al., 2012].

The constraints under which our equation (2.13) for α is derived are far less restrictive than those used in deriving Charney's QG equation (and we never need to assume isotropy).

In particular, one of *several constraints* needed for deriving Charney's QG equation is the scaling required for the potential temperature (his equation (3)), which written in terms of the potential density is

$$\frac{\tilde{\rho}}{\bar{\rho}} = -\frac{f}{g}\frac{\partial \psi}{\partial z}, \tag{2.19}$$

where ψ is the stream function of horizontal velocity. This constraint *alone* (which is effectively the thermal wind equation) implies our relationship (2.13) for α. To see this, in equation (2.19) replace

$$\psi \quad \text{with} \quad V_\theta L, \tag{2.20}$$

$$\frac{\partial}{\partial z} \quad \text{with} \quad \frac{1}{H}, \tag{2.21}$$

$$V_\theta \quad \text{with} \quad Rof L, \tag{2.22}$$

$$\frac{\tilde{\rho}}{\bar{\rho}} \quad \text{with} \quad \frac{H}{\bar{\rho}}\left[\left(\frac{\partial \rho}{\partial z}\right)_c - \frac{\partial \bar{\rho}}{\partial z}\right] = \frac{H}{g}\left(\bar{N}^2 - N_c^2\right). \tag{2.23}$$

With these replacements, equation (2.19) immediately gives

$$\left(\frac{H}{L}\right)^2 = Ro\,\frac{f^2}{N_c^2 - \bar{N}^2}, \tag{2.24}$$

which is the small Ro limit of equation (2.13).

Gill [1981] also proposed a relationship for α that differs from ours. He based his relation for α on a model 2D zonal flow (that is, not an axisymmetric vortex, but rather a 2D vortex) and found that α was proportional to

$$Ro\, f/\bar{N}.$$

To determine α, Gill derived separate solutions for the flow inside and outside his 2D model vortex, which he assumed was dissipationless and in geostrophic and hydrostatic balance. Despite the fact that Gill's published relation for α, obtained from the *outside* solution, differs from ours, we can show that his solution for the flow *inside* his 2D vortex satisfies our scaling relation for α: Gill's solution for the zonal velocity (which is in the y direction) is

$$v = -(f/a)x \tag{2.25}$$

(his equation (5.14) in dimensional form). His density anomaly is

$$\tilde{\rho} = \rho_o\,(\bar{N}^2/g)\,z \tag{2.26}$$

(i.e. within the 2D vortex, $\rho = \rho_o$). The equation for v gives $\omega_z = -(f/a)$, and therefore

$$Ro \equiv \frac{\omega_c}{2f} = -\frac{1}{2a} \tag{2.27}$$

Substituting v and $\tilde{\rho}$ into the equations for geostrophic and hydrostatic balance, gives

$$\frac{\partial \tilde{p}}{\partial x} = -\rho_o \frac{f^2}{a}\, x \tag{2.28}$$

and

$$\frac{\partial \tilde{p}}{\partial z} = -\rho_o\, \bar{N}^2\, z \tag{2.29}$$

respectively. Using the definitions of H and L from Section 2.2 along with $Ro = -1/(2a)$, we obtain

$$\alpha^2 = -Ro\, \frac{f^2}{\bar{N}^2}, \tag{2.30}$$

which is our relation (2.13) in the limit of small Ro, $L = R_v$, and $N_c = 0$ (which are the constraints under which Gill's solution is obtained). Gill's scaling for α is derived from the flow *outside* the vortex, which he derived by requiring that both the tangential velocity and density are continuous at the interface between the inside and outside solutions. In general, this *over–constrains* the dissipationless flow (which only requires pressure and normal velocity to be continuous – see for example the vortex solution in Aubert et al. [2012] in which the pressure and normal component of the velocity are continuous at the interface, but not the density or tangential velocity.) The extra constraints force the solution outside Gill's vortex to have additional (unphysical) length scales, resulting in Gill's relation for α differing from ours. Aubert et al. [2012] show that Gill's relationship for α does not fit their laboratory experiments, meddies, or Jovian vortices. We examine the accuracy of both Charney's and Gill's relationships in Section 2.7.

2.4 Gaussian Solution to the Dissipationless Boussinesq Equations

It is possible to find closed–form solutions to the steady, axisymmetric, dissipationless Boussinesq equations (e.g. [Aubert et al., 2012]). One solution that we shall use to generate initial conditions for our initial–value codes is the *Gaussian* vortex with

$$\tilde{p} = \tilde{p}_c \exp[-(z/H)^2 - (r/L)^2] \tag{2.31}$$

$$v_r = 0 \tag{2.32}$$

$$v_z = 0 \tag{2.33}$$

where $\tilde{p}_c$, H, and L are arbitrary constants. Then, $\tilde{\rho}$ is found from $\partial\tilde{p}/\partial z$ using equation (2.6), and v_θ is found from $\partial\tilde{p}/\partial r$ using equation (2.5) with ρ replaced by ρ_o. This Gaussian vortex exactly obeys our relationship (2.13) for α when the Rossby number is defined as before as

$Ro \equiv \omega_c/(2f)$, when R_v is set equal to L, and when the vertical and horizontal scales are defined as in Section 2.2. Note that $N(r,z)$ within the vortex is not uniform, that

$$N_c^2 = \bar{N}^2 - 2\tilde{p}_c/(\rho_o H^2), \tag{2.34}$$

and that the vortex is *shielded*. By *shielded*, we mean that there is a ring of cyclonic (anticyclonic) vorticity around the anticyclonic (cyclonic) core in each horizontal plane, and therefore at each z, circulation due to the vertical component of the vorticity is zero (i.e. the vortices are *isolated*). The Gaussian vortex could be a cyclone or an anticyclone depending on the choice of constants. This vortex is well-studied and has been widely used to model isolated vortices, especially in the oceans [e.g. Gent and McWilliams, 1986, Morel and McWilliams, 1997, Stuart et al., 2011].

Another model that is used frequently in studies of barotropic and baroclinic vortices is an axisymmetric vortex with a Gaussian vertical vorticity distribution [van Heijst and Clercx, 2009, eqs. 18]. The velocity field of this vortex is

$$v_\theta(r,z) = f\,Ro\,\frac{R^2}{r}\{1-\exp[-(r/R)^2]\}\exp[-(z/H)^2] \tag{2.35}$$

$$v_r = 0 \tag{2.36}$$

$$v_z = 0 \tag{2.37}$$

This vortex is unshielded and non–isolated. The pressure and density anomalies ($\tilde{p}$ and $\tilde{\rho}$) can be readily calculated from (2.5) and (2.6) in the geostrophic regime (i.e. v_θ^2 neglected). The length scales of the pressure anomaly (i.e. L and H), Ro, $N_c/\bar{N}$, and $f/\bar{N}$ are then found to satisfy the small Ro limit of (2.13) (i.e., equation (2.24))[2]. The velocity field of a non–isolated vortex decays slowly with r; as a result, simulations with horizontally periodic boundaries, such as the ones in section 2.5, have been found problematic for non–isolated vortices in the presence of stratification, where inertio–gravity waves propagate and reflect back from the boundaries. Therefore, non–shielded vortices are not studied numerically in Case A of section 2.5.

2.5 Numerical Simulation of the Boussinesq Equations

To use 3D numerical simulations to verify our relation (2.13) for α in a Boussinesq flow with constant $\bar{N}$ and f, we solve the equations of motion in a rotating-frame in Cartesian

[2]Note that $L \neq R$.

coordinates [Vallis, 2006]:

$$\nabla\cdot\mathbf{v} = 0 \tag{2.38}$$

$$\frac{D\mathbf{v}}{Dt} = -\frac{\nabla p}{\rho_o} + \mathbf{v}\times f\hat{\mathbf{z}} - \frac{\tilde{\rho}}{\rho_o}g\hat{\mathbf{z}} + \nu\nabla^2\mathbf{v} \tag{2.39}$$

$$\frac{D\tilde{\rho}}{Dt} = \rho_o\frac{\bar{N}^2}{g}w - \frac{\tilde{\rho}}{\tau_{rad}}, \tag{2.40}$$

where $D/Dt = \partial/\partial t + \mathbf{v}\cdot\nabla$, and $\mathbf{v} = (u, v, w)$ (Notice that throughout this paper, we use v_z and w for the vertical component of velocity in the cylindrical and Cartesian coordinates, respectively.) We include kinematic viscosity ν in equation (2.39), but neglect the diffusion of density because diffusion is slow (e.g., for salt-water the Schmidt number is ~ 700). Instead, inspired by astrophysical vortices (e.g., Jovian vortices or vortices of protoplanetary disks) for which thermal radiation is the main dissipating mechanism, we have added the damping term $-\tilde{\rho}/\tau_{rad}$ to the density equation in (2.40) to model *radiative dissipation*, where τ_{rad} is radiative dissipation time scale.

A pseudo–spectral method with 256^3 modes is used to solve equations (2.38)–(2.40) in a triply periodic domain (which was chosen to be 10 to 20 times larger than the vortex in each direction). Details of the numerical method is the same as [Barranco and Marcus, 2006]. Second–order Adams–Bashforth and Crank–Nicholson methods are used for time integration. For inviscid or high Reynolds number cases, hyperviscosity, similar to the one used by [Barranco and Marcus, 2006], is used. Because rotating stratified flows support inertio–gravity waves which reflect back from the periodic boundaries and interact with the vortex, if necessary, a small frictional Rayleigh layer (sponge layer) is added at the edges of the domain to damp wave reflections. The results of our triply periodic code are qualitatively, and in most cases quantitatively, the same as solutions we obtained with a code with no–slip vertical boundary conditions. That is because our vortices are far from the vertical boundaries, and therefore the Ekman circulation is absent.

2.6 Numerical Results for Vortex Aspect Ratios

As shown in table 2.1, we have examined the aspect ratios of vortices in four types of initial-value numerical experiments. The goal of these simulations is to determine how well the aspect ratios α of vortices obey our relation (2.13) as they evolve in time.

Case A: Run-Down Experiments

In this case, our initial condition is the velocity and density anomaly of the Gaussian vortex from Section 2.4 that is an exact equilibrium of the dissipationless Boussinesq equations with constant f and $\bar{N}$. These are "run-down" experiments because they are carried out *either* with radiative dissipation (i.e., finite τ_{rad}) *or* viscosity, but not both. Due to the

Case	$\tilde{N}/N_c$	H/L	τ_{rad}	Ro	$E_k(10^{-5})$
A1	1/0	16/8	∞	-0.2	25
A2	1/0	16/8	∞	-0.2	12.5
A3	1/0	16/8	∞	-0.2	6.25
A4	1/0.5	16/8	∞	-0.14	25
A5	1/0.5	4/2	∞	-0.14	25
A6	20/19.99	0.05/0.02	∞	-0.11	500
A7	1/0	20/12	∞	-0.12	11.1
A8	1/0	16/8	∞	-0.2	25
A9	1/0	12/12	∞	-0.04	11.1
A10	20/19.9	0.03/0.03	∞	-0.2	222.2
A11	20/19.9	0.03/0.03	∞	-0.2	11.1
A12	3.53/2.5	0.96/0.96	∞	-0.5	39.3
A13	3.54/3.45	0.96/0.96	∞	-0.023	39.3
A14	1.56/1.64	6.55/3.28	∞	$+0.0386$	3.91
A15	0.5/0.75	16/8	∞	$+0.0477$	4
A16	0.5/0.55	16/8	∞	$+0.0083$	4
A17	3.33/3.49	1.44/0.72	∞	$+0.15$	4
A18	3.33/3.17	1.44/0.72	∞	-0.22	4
A19	10/10.5	0.16/0.08	∞	$+0.87$	250
A20	3.33/3.49	1.44/0.72	1656	$+0.14$	0
A21	1/1.0475	16/8	1656	$+0.015$	0
A22	3.33/3.17	1.44/0.72	1237	-0.22	0
A23	3.33/3.49	1.44/0.72	120	$+0.14$	0
A24	3.33/3.17	1.44/0.72	120	-0.22	0
B1	1/0	20/12	∞	-0.12	4
B2	1/0	20/12	∞	-0.12	4
B3	1/0	20/12	∞	-0.12	0
C1	1/0.761	6.09/5.67	∞	$+0.33$	49.7
C2	1/0.709	5.91/5.67	∞	$+0.35$	45.9
D1	2.5/2.5	40/2	∞	-0.75	25.4
D2	2.5/2.5	40/2	∞	-0.75	12.7
D3	1.67/1.67	90/4.5	∞	-0.5	16.9
D4	5/5	10/0.5	∞	-1	50.7
D5	20/20	0.6/.03	∞	$+0.8$	24.4

Table 2.1: Parameters of the background flows and of the vortices at the "initial" time. For Cases A, B, and D the "initial" time is $t = 0$, and for Case C the "initial" time is $t = t_{off}$. All values are in CGS units. For all cases, $f = 5$ rad/s, $g = 980$ m/s^2, and $\rho_o = 1$ g/cm^3. Ekman number is defined as $E_k \equiv \nu/(fL^2)$. See text for the difference between Cases B1 and B2. For Case C1, $t_{off} = 60$ s and $Q = -64$ cm^3/s, and for Case C2, $t_{off} = 30$ s and $Q = -128$ cm^3/s.

weak dissipation, the vortices slowly evolve (decay) and do not remain Gaussian. Also, as a result of the dissipation (and decay), a weak secondary flow is induced (i.e. non-zero v_r and v_z). The secondary flows and their roles are further discussed in Chapter 3, Marcus and Hassanzadeh [2011], and Hassanzadeh and Marcus [2012].

Case B: Vortices Generated by Geostrophic Adjustment

This case is motivated by vortices produced from the geostrophic adjustment of a locally mixed patch of density, e.g. generated from diapycnal mixing [see e.g. McWilliams, 1988, Stuart et al., 2011]. Our flow is initialized with $\mathbf{v} = 0$ and $\tilde{\rho} \neq 0$. For Cases B1 and B3 the initial $\tilde{\rho}$ is that of the Gaussian vortex discussed in Section 2.4. But here, the initial flow is far from equilibrium because $\mathbf{v} \equiv 0$. In Case B2, the initial $\tilde{\rho}$ is Gaussian in r, but has a top-hat function in z (for this case, the initial H is defined as the half-height of the top-hat function). It is observed in the numerical simulations that geostrophic adjustment quickly produces shielded vortices.

Case C: Cyclones Produced by Suction

Injection of fluid into a rotating flow generates anticyclones [Aubert et al., 2012], while suction produces cyclones. We simulate suction by modifying the continuity equation (2.38) as

$$\nabla \cdot \mathbf{v} = Q(\mathbf{x}, t) \tag{2.41}$$

where Q is a specified suction rate function and $\mathbf{x} = (x, y, z)$. The flow is initialized with $\mathbf{v} = \tilde{\rho} = 0$. Suction starts at $t = 0$ over a spherical region with radius of 6 cm and is turned off at time t_{off}. A shielded cyclone is produced and strengthened during the suction process. As mentioned at the end of Section 2.2, for $Ro > 0$, relation (2.13) requires the flow to be superstratified (i.e. $N_c > \bar{N}$). Our numerical simulations show that the initial suction creates super–stratification. Cases C1 and C2 have different suction rates and t_{off}, but the same total sucked volume of fluid, and it is observed that the produced cyclones are similar. The dynamics of cyclones produced by localized suction are explored in details in Chapter 3.

Case D: Vortices Produced from the Breakup of Tall Barotropic Vortices

The violent breakup of tall barotropic (z-independent) vortices in rotating stratified flows can produce stable compact vortices [see e.g. Smyth and McWilliams, 1998]. In Case D, our flows are initialized with an unstable 2D columnar vortex with

$$v_\theta = Ro\, f\, r \exp(-(r/L)^2) \tag{2.42}$$

and $\tilde{\rho} = 0$ (for this case, the initial H is the vertical height of the computational domain). Note that the initial columnar vortex is shielded. Noise is added to the initial velocity field

to hasten instabilities. The vortex breaks up and then the remnants equilibrate to one or more compact shielded vortices (Figure 2.1). In each case, only the vortex with the largest $|Ro|$ is analyzed in Section 2.7.

2.7 Aspect Ratio: Numerical Simulations

In all cases, vortices reach quasi-equilibrium and then slowly decay due to viscous or radiative dissipation except for Case B3 which is dissipationless and evolves only due to geostrophic adjustment. As a result, Ro decreases, and the mixing of density in the vortex interior changes (i.e., N_c changes). Therefore, it is not surprising that the aspect ratio α also changes in time. Quasi-equilibrium is reached in Case A almost immediately. In Case B, vortices quickly form and come to quasi-equilibrium after geostrophic adjustment. Quasi-equilibrium is achieved following the geostrophic and hydrostatic adjustments after t_{off} in Case C, and (much longer) after the initial instabilities in Case D.

For each case, we use the results of the numerical simulations to calculate

$$Ro(t) \equiv \frac{\omega_c(t)}{2f} \tag{2.43}$$

and

$$N_c(t) \equiv \sqrt{\bar{N}^2 - \frac{g}{\rho_o}\left(\frac{\partial \tilde{\rho}(\mathbf{x},t)}{\partial z}\right)_c} \tag{2.44}$$

We compute $L(t)$ and $H(t)$ from the numerical solutions using their definitions given in Section 2.2. Calculating L based on $\nabla_\perp^2$ rather than just r-derivatives is useful for non-axisymmetric vortices. For example, due to a small non-axisymmetric perturbation added to the initial condition of Case A8, the vortex went unstable and produced a tripole [van Heijst and Kloosterziel, 1989]. Cases C1 and C2 also produced non-axisymmetric vortices. We define the *numerical* aspect ratio as

$$\alpha_{\mathrm{NUM}}(t) \equiv \frac{H(t)}{L(t)}. \tag{2.45}$$

We define the *theoretical* aspect ratio α_{THR} from equation (2.13) using $Ro(t)$ and $N_c(t)$ extracted from the numerical results and the (constant) values of f and $\bar{N}$.

Figure 2.2 shows how well α_{THR} agrees with α_{NUM}. The inset in Figure 2.2 shows that the relative difference between the two values, calculated as

$$|1 - (\alpha_{\mathrm{NUM}}/\alpha_{\mathrm{THR}})^2|,$$

is smaller than 0.07. For each case, the maximum difference occurs at early times or during instabilities.

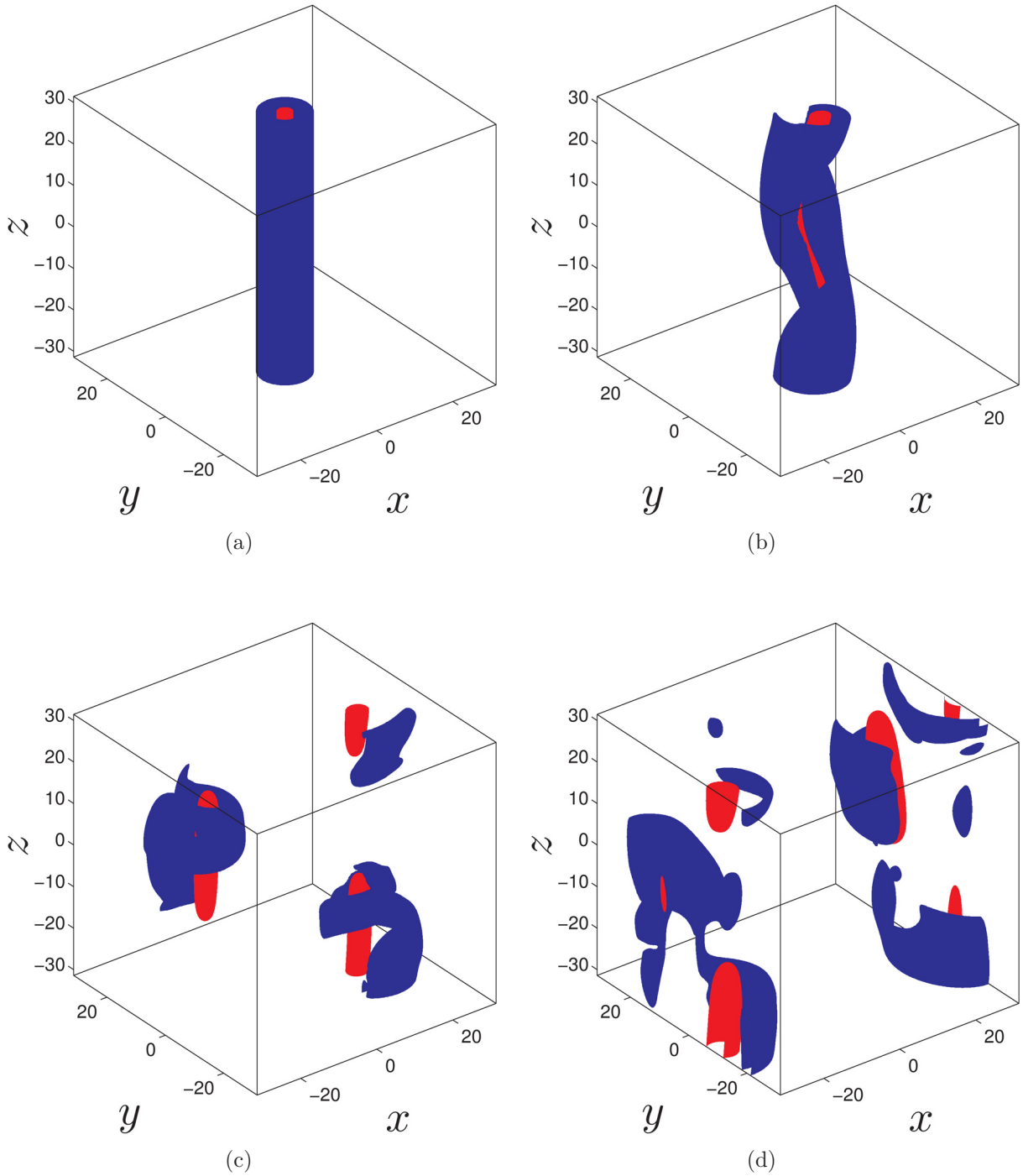

Figure 2.1: Isosurfaces of $0.5\max(\omega_z)$ (blue) and $0.5\min(\omega_z)$ (red) for Case D1 at (a) $t/T = 0$, (b) $t/T = 60$, (c) $t/T = 120$, and (d) $t/T = 240$, where $T = 4\pi/f$ is the inertial period.

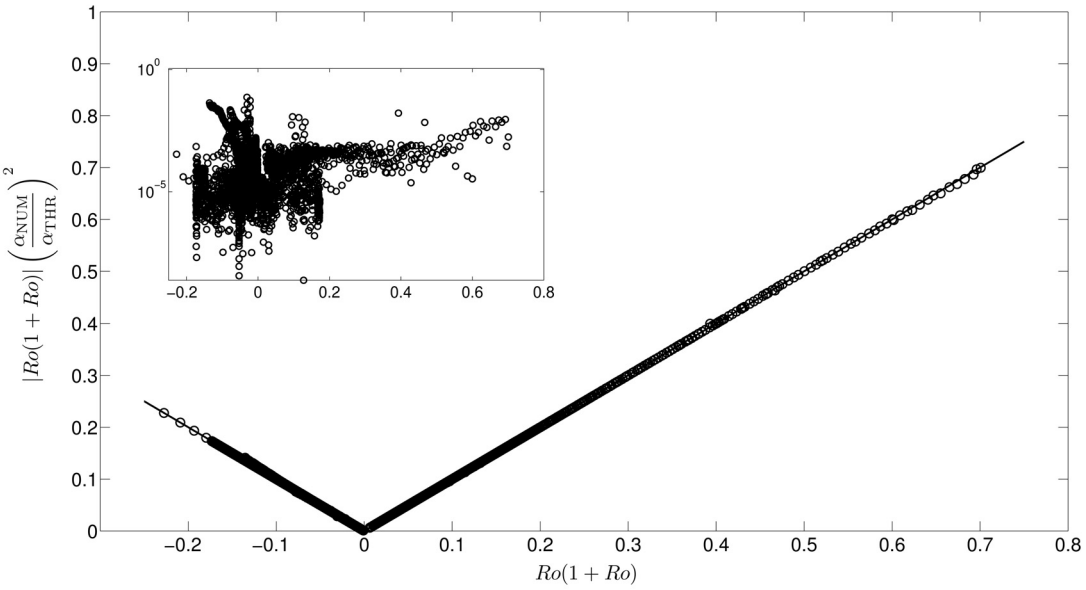

Figure 2.2: Comparison of $\alpha_{\rm NUM}$ with $\alpha_{\rm THR}$ (see text for definitions). The circles show the value of $|Ro(1+Ro)|(\alpha_{\rm NUM}/\alpha_{\rm THR})^2$ and the straight lines show the value of this expression if $\alpha_{\rm NUM} \equiv \alpha_{\rm THR}$. All 4122 data points (circles) collapse on the straight lines (and densely cover them), validating our equation (2.13). Data points are recorded one inertial period ($= 4\pi/f$) after the initial time (as defined in table 2.1) in Cases A-C, and 50 inertial periods after $t = 0$ in Case D. Note that all of our simulated vortices have $L = R_v$. The horizontal axis in the inset is the same as in the main Figure; the inset's vertical axis is the relative difference $|1 - (\alpha_{\rm NUM}/\alpha_{\rm THR})^2|$ (which is < 0.07). (*n.b.*, the left-most plotted point has $Ro(1+Ro) \simeq -0.25$ due to the mathematical tautology that $Ro(1+Ro) \geq -0.25$ for all values of Ro.)

Figure 2.3 compares the values of $\alpha_{\rm NUM}$ with $\alpha_{\rm THR}$ as a function of time for six cases. The Figure starts at time $t = 0$, so it includes vortices which are not in CG-H equilibrium to examine the situations for which relationship (2.13) for α may *not* be good due to transients. Cases A1, B1, and A20 in Figure 2.3a exhibit excellent agreement with our theoretical prediction for α, while Case A8 shows a small deviation starting around $t = 80(4\pi/f)$. This deviation is a result of the vortex going unstable at this time (accompanying by relatively large v_r and v_z) and forming a tripolar vortex. After the tripole comes to CG-H equilibrium, its α once again agrees with theory. As the vortices dissipate, and Ro and N_c change, α can either decrease in time (c.f., Case A1) or increase (c.f., Case A20).

Figure 2.3b shows Cases D1 and D3 from time $t = 0$. The remnant vortices that formed from the violent break-up of the columnar vortices are initially far from the CG-H balance. As a result, the value of $\alpha_{\rm THR}$ at these early times does not fit well with the values of

α_{NUM}. However, after the CG-H balance is established in the remnants, our theoretical relationship (2.13) becomes valid and α_{THR} agrees well with α_{NUM}.

Figure 2.3a shows that the alternative scaling relation based on Charney's QG equation, $\alpha = f/\bar{N}$, is not a good fit to our numerical data. Cases A1, A8, and B1 all have $f/\bar{N} = 5$ which is obviously far from the measured aspect ratio of these vortices. Case A20 has $f/\bar{N} = 1.5$ which again does not agree with α_{NUM}. In fact, in all four cases, the difference between $\alpha_{\mathrm{NUM}}(t)$ and $f/\bar{N}$ increases with time, while $\alpha_{\mathrm{THR}}(t)$ always remains close to $\alpha_{\mathrm{NUM}}(t)$. For other cases in table 2.1, it has been observed that for vortices which are in CG-H equilibrium, $\alpha_{\mathrm{NUM}}/(f/\bar{N})$ can be as large as 9.56 and as small as 0.11. The data displayed in Figure 2.3b were carefully "cherry-picked" from all of our runs because they are unusual in that $\alpha \to f/\bar{N}$ after a long time. The fluid within the remnants strongly mixed with the background fluid, so at late times $N_c \to \bar{N}$ and Ro significantly decreases and therefore the conditions needed for the validity of Charney's QG equation are approached. Whether these results are a fluke and whether $\alpha \to f/\bar{N}$ for all vortices that are created in *one particular case* is not yet clear. The physics governing these vortices is currently be investigated and will be discussed in a future paper.

Gill's relation for α, discussed in Section 2.3, is not a good fit to any of our numerically computed vortices. For example, the value of $\alpha_{\mathrm{NUM}}(t)/(Ro(t)f/\bar{N})$ is between 2 and 8 for Case A1; 2 and 9 for Case A8; 80 and 160 for Case A20; and 4 and 7 for Case B1. The much larger error observed for Case A20 is due to the fact that unlike the other three cases, N_c is far from 0 in this case, and Gill's derivation does not incorporate $N_c \neq 0$.

2.8 Conclusion

We have derived a new relationship (2.13) for the aspect ratio α of baroclinic vortices in cyclo–geostrophic and hydrostatic (CG-H) equilibrium and used numerical initial-value simulations of the Boussinesq equations to validate this relation for a wide variety of unforced quasi-steady vortices generated and dissipated with different mechanisms. Our new relationship shows that α depends on the background flow's Coriolis parameter f and Brunt-Väisälä frequency $\bar{N}$, as well as properties of the vortex, including Ro and N_c. Thus, it shows that all vortices embedded in the same *background* flow do *not* have the same aspect ratios. In a companion paper, [Aubert et al., 2012] verify the new relationship with laboratory experiments and show it to be consistent with observations of Atlantic meddies and Jovian vortices.

Equation (2.13) for α has several consequences. For example, it shows that for cyclones ($Ro > 0$), N_c must be greater than $\bar{N}$, that is, the fluid within a cyclone must be *super-stratified* with respect to the background stratification. Mixing usually de-stratifies the flow over a local region, and therefore cannot produce cyclones. This may explain why there are more anticyclones than cyclones observed in nature. We numerically simulated local suction to create cyclones, and we found that suction creates a large envelope of super-stratified flow around the location of the suction and when the suction is stopped, the CG-H adjustment

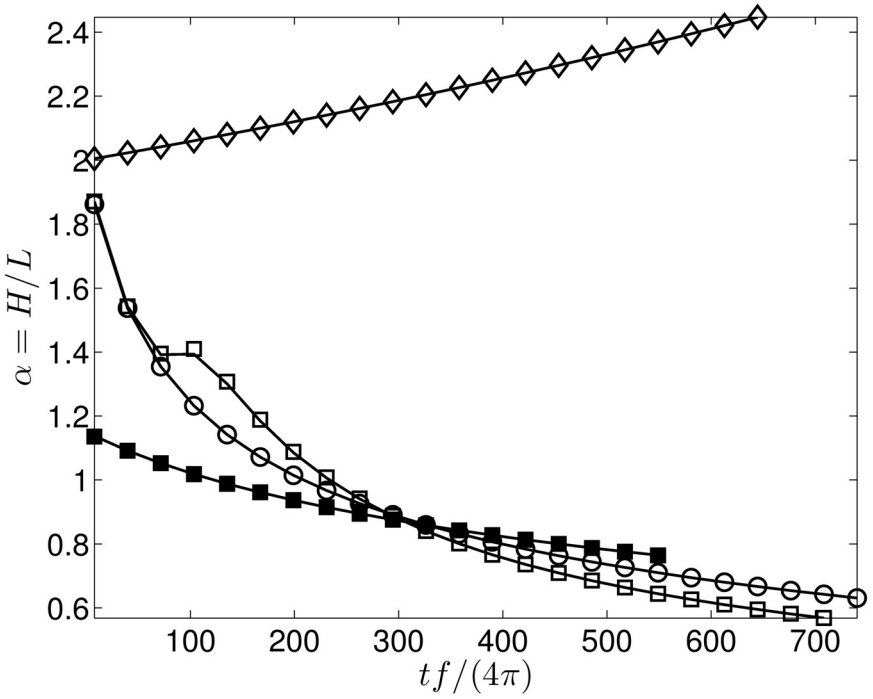

(a)

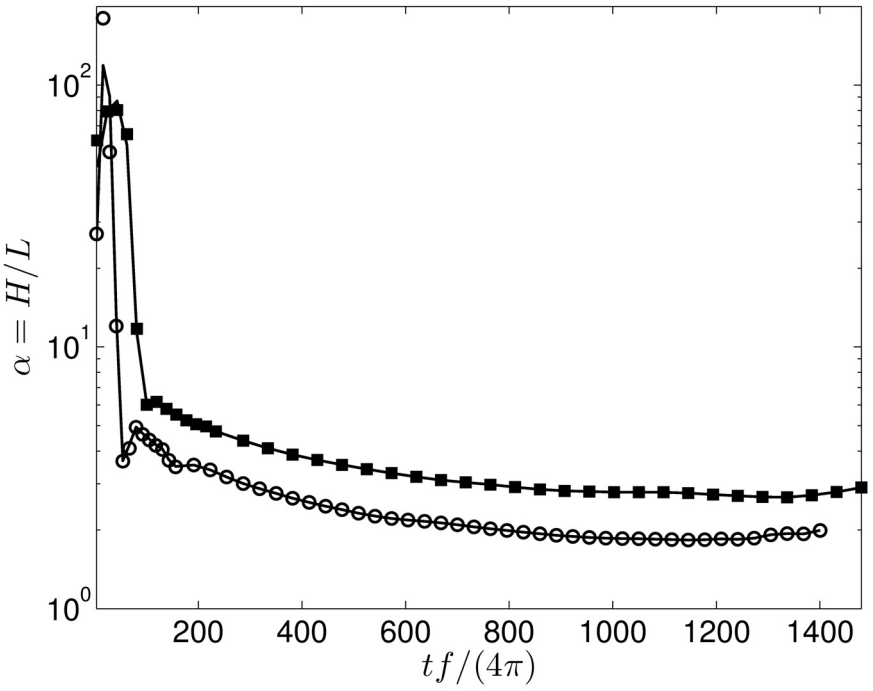

(b)

Figure 2.3: Time evolution of $\alpha_{\rm THR}$ (continuous curves), and $\alpha_{\rm NUM}$ for Cases (a) A1 $\circ$, A8 $\square$, B1 $\blacksquare$, and A20 $\diamond$, (b) D1 $\circ$, and D3 $\blacksquare$. Cases A1, A8 and B1 have $f/\bar{N} = 5$ and Case A20 has $f/\bar{N} = 1.5$ which differ significantly from α. Case D1 has $f/\bar{N} = 2$ and Case D3 has $f/\bar{N} = 3$ which agree with α only at the late times.

makes cyclones. Details of these simulations and results of an ongoing laboratory experiment will be presented in subsequent publications.

It is widely quoted that vortices obey the quasi-geostrophic scaling law $\alpha = f/\bar{N}$ (i.e. Burger number $Bu = 1$). This is inconsistent with our relationship which written in terms of Bu is

$$Bu = \frac{Ro(1+Ro)}{(N_c/\bar{N})^2 - 1} \tag{2.46}$$

We found that, with the exception of one family of vortices, the quasi-geostrophic scaling law was not obeyed by the vortices studied here (and by Aubert et al. [2012]), and could be incorrect by more than a factor of 10. Another relationship proposed by Gill [1981] was also found to produce very poor predictions of aspect ratio.

We found that α can either increase or decrease as the vortex decays, and our relationship (2.13) shows that the dependence of α on N_c is specially sensitive when N_c is at the order of $\bar{N}$, as it is for meddies and Jovian vortices [Aubert et al., 2012]. Our simulations showed that N_c was determined by the secondary circulations within a vortex and that those circulations are controlled by the dissipation. In a future paper we shall report on the details of how dissipation determines the secondary flows and the temporal evolution of N_c, both of which are important in planetary atmospheres, oceanic vortices, accretion disk flows, and planet formation [Barranco and Marcus, 2005].

Chapter 3

Baroclinic Cyclones Produced by Localized Suction

3.1 Introduction

Vortices that swirl in the same (opposite) direction as (of) the background rotation are called cyclones (anticyclones). Both cyclones and anticyclones exist in the oceans [Olson, 1991], but large long–lived vortices are predominantly anticyclonic [see e.g. McWilliams, 1985, Sangrà et al., 2009, Perret et al., 2011]. Cyclones and anticyclones also exist in the atmosphere of Jupiter [Vasavada and Showman, 2005] and Saturn [Sayanagi et al., 2010], but large long–lived vortices are mostly anticyclonic [Mac Low and Ingersoll, 1986, Cho and Polvani, 1996b]. For example, Jupiter's Great Red Spot and White Ovals [Marcus, 1993], Red Oval [Go et al., 2006], and Neptune's Great Dark Spot [Smith et al., 1989] are all anticyclones.

The cyclone–anticyclone asymmetry is also observed in experimental and numerical studies and has received considerable attention in recent years. In rotating constant–density flows, cyclones and anticyclones form 2D Taylor columns and their dynamics differ due to the ageostrophic effects. Most numerical and laboratory studies found cyclonic predominance in strongly rotating constant–density flows [see Moisy et al., 2010, and references therein]. On the other hand, the cyclone–anticyclone asymmetry in rotating stratified flows, where vortices are essentially 3D [Hassanzadeh et al., 2012, Aubert et al., 2012], is still controversial. Most numerical simulations of shallow–water or primitive equations [Polvani et al., 1994, Cho and Polvani, 1996a, Koszalka et al., 2009] and laboratory experiments [Linden et al., 1995, Perret et al., 2006] have shown the predominance of coherent anticyclones in

With minor modifications, Chapter 3 appears in:
P. Hassanzadeh, O. Aubert, P. S. Marcus, M. Le Bars, and P. Le Gal, *Three–Dimensional Cyclones Produced by Localized Suction in Rotating Stratified Flows: a Numerical and Experimental Study*, to be submitted to the Journal of Fluid Mechanics, 2013.

rotating stratified flow. (Note that the quasi–geostrophic equations are degenerate with respect to the cyclone–anticyclone asymmetry, see e.g. Pedlosky [1990].) In contrast to these studies, some laboratory experiments [Praud et al., 2006] and numerical simulations with boundary dynamics [Hakim et al., 2002, Roullet and Klein, 2010] have reported cyclonic predominance.

The dominance of anticyclones in most simulations, experiments, and observations can be due to one or more of the following: (1) the creation mechanisms favor anticyclones over cyclones [McWilliams, 1985, Perret et al., 2011], (2) anticyclones are more stable than cyclones [Stegner and Dritschel, 2000, Graves et al., 2006], (3) anticyclones are easier to observe [Marcus, 2004], (4) anticyclones have greater longevity compared to cyclones, and (5) cyclones exist in a smaller parameter regime than anticyclones. All of these possibilities, in particular the last two, need further investigation.

Cyclones have low–pressure centers so that in a horizontal plane, the radially inward pressure force balances the radially outward Coriolis and centrifugal forces [Kundu and Cohen, 2010]. To support the low–pressure core in the vertical, a baroclinic cyclone must have an interior more stratified than the surrounding flow, so that the buoyancy force balances the pressure force [Hassanzadeh et al., 2012, Aubert et al., 2012, also see Section 3.6]. Conversely, baroclinic anticyclones in geostrophic balance have high–pressure cores and interiors less stratified than their environments. Therefore, the dynamics of cyclones and anticyclones in strongly rotating stratified flows differ not only because of the nonlinear effects, but also because of their dissimilar internal stratification. The consequences of the latter for the stability and longevity of the vortices has not been fully explored.

A region that is more stratified than the background flow (e.g., inside a cyclone) is called *super–stratified* hereafter. For a process to produce cyclones in near cyclo–geostrophic and hydrostatic balances, a super–stratified region has to be created. It has been suggested by Hassanzadeh et al. [2012] and Aubert et al. [2012] that the super–stratification requirement may be a key factor in the sparsity of cyclones, because mixing, which is ubiquitous in nature because of turbulence, tends to de–stratify the flow and produces regions of less stratification, and therefore favor anticyclones [McWilliams, 1985, 1988].

Localized suction (injection) is one of the standard methods used in laboratory experiments for producing barotropic cyclones (anticyclones) in rotating flows with constant–density [van Heijst and Clercx, 2009]. In rotating stratified flows, local injection of a constant density fluid has been used to produce 3D baroclinic anticyclones [Griffiths and Linden, 1981, Hedstrom and Armi, 1988, Bush and Woods, 1999, Aubert et al., 2012]. However, suction has not been used previously as a method of creating local super–stratification, and with the exception of Linden et al. [1995] and Cenedese and Linden [1999], has not been used to produce cyclones in rotating stratified laboratory flows. In analytic and numerical studies using the linearized Boussinesq [McDonald, 1992], shallow–water [Davey and Killworth, 1989, Aiki and Yamagata, 2000, 2004], or quasi–geostrophic [Hines, 1997] equations, localized sources and sinks have been used to model buoyancy–driven circulation in the deep ocean and to model the generation of oceanic vortices.

In this paper we show that 3D baroclinic cyclones can be produced by localized suction

in a rotating, continuously stratified flow in both laboratory experiments and numerical simulations. The purpose of this paper is to obtain a better understanding of how localized suction produces cyclonic vorticity and super–stratification. Such physical understanding is key in designing experimental studies of cyclones, of the cyclone–anticyclone asymmetry, and also in the investigation of natural processes that are modeled as localized sinks. Additionally, we investigate the dynamics of viscously decaying cyclones and the evolution of their super–stratified interior and meridional velocities (i.e., secondary circulation). The remainder of this section discusses why suction and injection are distinct phenomena and not the time–reverse of each other. In Section 3.2 we present the experimental setup, and in Section 3.3 we rederive the Boussinesq equations to account for localized suction. Section 3.3 also briefly reviews the numerical method used to solve these equations. Section 3.4 shows how rotation and stratification affect the symmetries of the flow. Sections 3.5 and 3.6 discuss the details of the flow field during suction and after the suction stops, respectively. Section 3.7 presents our conclusion and plans for future work.

Suction versus Injection

We remind the reader that the suction/injection of viscous fluids from an orifice is not time-reversible, and suction is therefore *not* the time–reverse of injection. Viscosity plays an important role in injection, particularly at the tip of the orifice where it forms a vortex sheet around a jet–like flow. On the other hand, suction has a more global effect: the fluid moves toward the orifice from all directions, regardless of the orientation of the orifice [also see Linden et al., 1995]. As a result, a candle can be easily put out by blowing air, but not (easily) by sucking air. Another manifestation of the suction–injection asymmetry is the reverse sprinkler, i.e. a lawn sprinkler submerged in a pool of water sucking the water in. A question raised by Ernest Mach and popularized by Richard Feynman in his memoir *Surely You're Joking, Mr. Feynman!*, a reverse sprinkler in fact does not rotate because of the absence of jets that produce torque in regular sprinklers to overcome the friction of the bearings [see Jenkins, 2004, for further discussion and historical accounts]. This understanding of suction will be exploited in Section 3.3 to derive the governing equations modified for localized suction.

3.2 Laboratory Experiment

A rotating tank partially filled with linearly stratified salt–water is used in the laboratory experiments (Figure 3.1). The apparatus is the same one used in Aubert et al. [2012] to produce anticyclones by local injection. The square tank is $50 \times 50 \times 70$ cm (all units in this papers are in cgs). The Oster double–bucket method is used to produce a 30 cm deep layer of linearly stratified fluid around the midplane with density profile $\bar{\rho}(z) = \rho_o[1 - \bar{N}^2(z - 15)/g]$, where $\bar{N}$ is the Brunt–Väisälä frequency and is constant in each experiment, g is the acceleration of gravity, ρ_o is the density of pure water, and z is the vertical coordinate

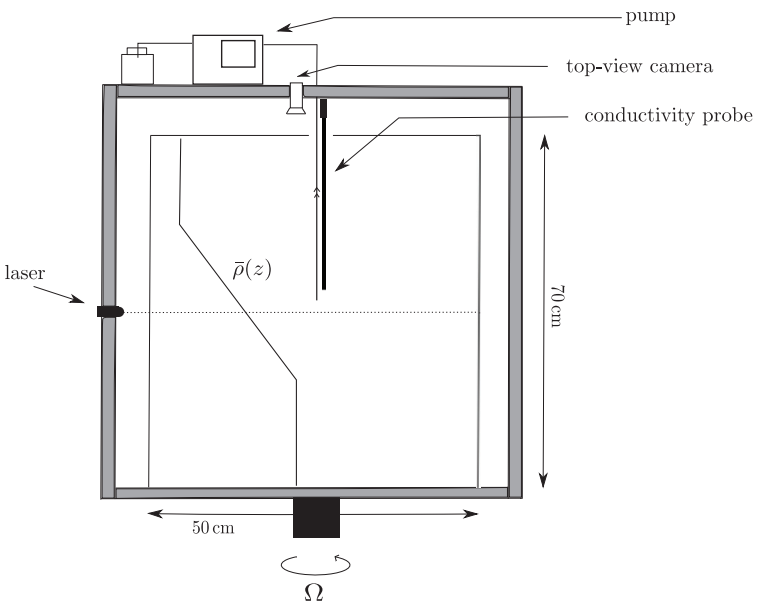

Figure 3.1: Schematic of the experimental setup: the $50 \times 50 \times 70$ cm tank is fixed on a rotating table and filled with salt–water, linearly stratified in the 30 cm middle layer. A pipe linked to a pump and a conductivity probe are mounted atop the tank and can translate vertically along the axis of rotation of the tank using separate motors. A horizontal laser sheet in the midplane (shown as a dotted line) and a top–view camera allows for recording and PIV measurements. Not shown are a side–view camera and a random dots pattern (on the opposite side of the tank facing the camera) for synthetic schlieren visualization.

measured from the middle of the tank. There is a 20 cm layer of pure water above the stratified layer. The Coriolis parameter f is twice the rotation rate of the tank. As shown in Figure 3.1, a pumping device is mounted on the top of the tank and is connected to a pipe that goes down to the middle of the stratified fluid $z = 0$ along the axis of rotation of the tank. The pipe has a diameter of 0.25 cm and can be moved vertically by a motor.

The entire stratified fluid is seeded with 30 μm particles. Particle Image Velocimetry (PIV) is employed to measure the velocity field in the rotating frame in horizontal planes. A microscale high–frequency conductivity probe [Head, 1983], also controlled by a motor mounted atop the tank, can be moved vertically in the stratified fluid. The conductivity probe is placed 0.7 cm off the axis of rotation and 1.5 cm above the midplane $z = 0$. Assuming the stratification to be linear between the midplane and the location of the probe and that the density at the midplane remains $\bar{\rho}(0)$, the density gradient is calculated from the conductivity measurements. The synthetic schlieren technique [Dalziel et al., 2000] is used to visualize density gradients in vertical planes. Even though the width of the tank is large compared to the radii of the produced cyclones and the flow is 3D, the good agreement between the density gradients measured with the synthetic schlieren technique and with the probe allows us to use the non–intrusive synthetic schlieren measurements when the probe

cannot be used because it disturbs the vortex.

Once the stationary tank is filled with the linear stratification, the tank is rotated at a fixed rate and the fluid is spun up to achieve *near* solid–body rotation (note that *exact* solid–body rotation cannot be achieved in the presence of diffusion, see e.g. von Zeipel [1924] and Greenspan [1990, pp. 12]). At this time, marked as $t = 0$, the pipe is moved down vertically along the center line of the tank to the midplane of the stratified fluid (i.e., $z = 0$). Fluid is then sucked out of the tank at a given volumetric rate Q_o [cm^3/s] for t_s seconds. After suction stops, the pipe is slowly removed from the fluid. Measurements are done both during and after the suction period.

3.3 Mathematical Formulation and Numerical Simulation

In this section we present 3D Boussinesq equations modified to account for localized suction of (continuously) stratified fluids. Although the equations are derived in the context of a laboratory experiment (i.e., suction is through a vertical pipe and the fluid is salt–water), the final equations are also suitable for modeling sinks (and sources) in oceans. The pseudo–spectral method that was used to solve these equations is described at the end of this section.

Let M be the mass of the salt–water in some infinitesimal volume V; M_s be the mass of the salt in the same volume; ρ be the local mass density of the salt–water; ρ_s be the local mass density of the salt; and ρ_w be the local mass density of pure water. Then $\rho = M/V$; $\rho_s = M_s/V$; and $\rho_w = M_w/V$. Thus,

$$\rho = (M_s + M_w)/V = \rho_s + \rho_w \tag{3.1}$$

We shall use the approximation that when salt is dissolved into pure water, the volume of the mixed fluid does not change significantly. Then $\rho_o \equiv \rho_w$ is constant in space and time, but $\rho(\mathbf{x}, t)$ and $\rho_s(\mathbf{x}, t)$ are functions of space and time ($\mathbf{x} = (x, y, z)$).

Conservation of the mass of water and salt, ignoring the diffusion of salt, requires

$$\frac{\partial \rho_w}{\partial t} = -\nabla \cdot (\rho_w \mathbf{v}) + \dot{S}_w \tag{3.2}$$

$$\frac{\partial \rho_s}{\partial t} = -\nabla \cdot (\rho_s \mathbf{v}) + \dot{S}_s \tag{3.3}$$

where $\dot{S}_s(\mathbf{x}, t)$ and $\dot{S}_w(\mathbf{x}, t)$ are the rates at which water and salt are being removed from the tank by the suction through the tip of the pipe, which is modeled here as a small but finite-sized spherical sink (see below). $\mathbf{v}(\mathbf{x}, t) = (u, v, w)$ is the 3D velocity field. Because ρ_w is constant ($= \rho_o$), the first equation simplifies to

$$\nabla \cdot \mathbf{v} = \dot{S}_w/\rho_o \tag{3.4}$$

Adding equations (3.2) and (3.3), and using the definition of total density ρ gives

$$\frac{\partial \rho}{\partial t} = -\nabla \cdot (\rho \mathbf{v}) + \dot{S} \tag{3.5}$$

where $\dot{S} = \dot{S}_w + \dot{S}_s$ is the total rate at which salt–water is sucked from the tank.

The pipe removes water and salt simultaneously, and we assume that the mass fraction of the salt that is removed by the pipe is equal to the local mass fraction of salt at the tip of the pipe. Therefore

$$\frac{\dot{S}}{\rho} = \frac{\dot{S}_s}{\rho_s} = \frac{\dot{S}_w}{\rho_o} \tag{3.6}$$

As a result, (3.4) becomes

$$\nabla \cdot \mathbf{v} = \dot{S}/\rho \equiv q(\mathbf{x}, t), \tag{3.7}$$

where $q(\mathbf{x}, t)$ is localized in space (see Section 3.3). Using equation (3.7) in (3.5) gives

$$\frac{\partial \rho}{\partial t} = -(\mathbf{v} \cdot \nabla)\rho - \rho(\dot{S}/\rho) + \dot{S} = -(\mathbf{v} \cdot \nabla)\rho \tag{3.8}$$

or

$$D\rho/Dt = 0 \tag{3.9}$$

where $D/Dt \equiv \partial/\partial t + \mathbf{v} \cdot \nabla$. Unlike equation (3.7), the density equation (3.9) is not modified by suction and does not include q.

The balance of momentum in an inertial frame gives

$$\frac{\partial(\rho \mathbf{v})}{\partial t} = -\nabla \cdot (\rho \mathbf{v}\mathbf{v}) - \nabla p + \rho q \mathbf{v} - \rho g \hat{\mathbf{z}} + \mu \nabla^2 \mathbf{v} \tag{3.10}$$

where p is the pressure, $\hat{\mathbf{z}}$ is the unit vector in the z direction, and μ is the dynamic viscosity. The third term on the right–hand side of (3.10) accounts for the loss of momentum through the pipe because we assumed that removing a parcel of fluid by the pipe also removes (from the domain) the momentum that the parcel carries. Note that because of the global effect of suction, discussed in Section 3.1, the sink term $\rho q \mathbf{v}$ does not have any directional preference imposed by the orientation of the pipe[3]. Exploiting (3.7) and (3.9), equation (3.10) reduces to

$$\rho \frac{D\mathbf{v}}{Dt} = -\nabla p - \rho g \hat{\mathbf{z}} + \mu \nabla^2 \mathbf{v} \tag{3.11}$$

[3]As a result, equation (3.10) is not appropriate to model injection from an orifice, but it can still be used to study some of the oceanic phenomena that can be modeled as a localized source. One example is the formation of Meddies through heavier Mediterranean water sinking in the Atlantic ocean [Zenk and Armi, 1990, Aiki and Yamagata, 2004].

Like the density equation (3.9), the momentum equation (3.11) is not changed by suction.

Consistent with previous approximations, we shall assume that the amount of the dissolved salt is very small (i.e., $M_s \ll M_w$). Therefore, $\rho_s \ll \rho_o$, which allows us to use the Boussinesq approximation [Kundu and Cohen, 2010]. Therefore, we neglect the departure of ρ from ρ_o in the momentum equation (3.11) except when multiplied by g:

$$\rho_o \frac{D\mathbf{v}}{Dt} = -\nabla\tilde{p} - \tilde{\rho}g\hat{\mathbf{z}} + \mu\nabla^2\mathbf{v} \tag{3.12}$$

where $\tilde{p}(\mathbf{x},t) \equiv p(\mathbf{x},t) - \bar{p}(z)$ and $\tilde{\rho}(\mathbf{x},t) \equiv \rho(\mathbf{x},t) - \bar{\rho}(z)$ are respectively the pressure and density anomaly, and $d\bar{p}/dz = -\bar{\rho}g$. Writing the density equation (3.9) in terms of $\tilde{\rho}$

$$\frac{D\tilde{\rho}}{Dt} = \rho_o w \frac{\bar{N}^2}{g} \tag{3.13}$$

where $\bar{N} \equiv \sqrt{-g(d\bar{\rho}/dz)/\rho_o}$.

In a frame rotating with uniform angular velocity $f/2$ around the z axis, equations (3.7) and (3.13) remain the same, and (3.12) is modified by the Coriolis force and becomes

$$\rho_o \frac{D\mathbf{v}}{Dt} = -\nabla\tilde{p} + \rho_o\mathbf{v}\times f\hat{\mathbf{z}} - \tilde{\rho}g\hat{\mathbf{z}} + \mu\nabla^2\mathbf{v} \tag{3.14}$$

where $\mathbf{v}$ is the (relative) velocity in the rotating frame hereafter, but the notation has not been changed for convenience[4]. Equations (3.7), (3.13), and (3.14) are consistent with the equations used by Davey and Killworth [1989] and McDonald [1992].

Taking the curl of equation (3.14) gives an equation for relative vorticity $\boldsymbol{\omega} \equiv \nabla\times\mathbf{v}$:

$$\frac{D\boldsymbol{\omega}}{Dt} = (\boldsymbol{\omega}\cdot\nabla)\mathbf{v} + f\frac{\partial\mathbf{v}}{\partial z} - (\boldsymbol{\omega} + f\hat{\mathbf{z}})q - \frac{g}{\rho_o}\nabla\times\tilde{\rho}\hat{\mathbf{z}} + \nu\nabla^2\boldsymbol{\omega} \tag{3.15}$$

where f is assumed constant (f–plane approximation) and $\nu = \mu/\rho_o$. Using equation (3.7), the vertical component of this equation simplifies to

$$\frac{D\omega_z}{Dt} = (\boldsymbol{\omega}_\perp\cdot\nabla_\perp)w - (\omega_z + f)(\nabla_\perp\cdot\mathbf{v}_\perp) + \nu\nabla^2\omega_z \tag{3.16}$$

where subscript $\perp$ means the horizontal component. Note that by definition, cyclones (anticyclones) have $f\omega_z > 0$ (< 0) in their cores.

[4]The deflection of the isopycnals of $\bar{\rho}$ from horizontal planes as a result of rotation is ignored assuming that the centrifugal buoyancy is much smaller than the gravitational buoyancy, see e.g. Hassanzadeh et al. [2012].

Numerical Method

A pseudo–spectral method is used to solve equations (3.7), (3.13), and (3.14) in Cartesian coordinates in a spatially triply periodic domain of size $(2D)^3$. Details of the numerical method are the same as Hassanzadeh et al. [2012]. Second–order Adams–Bashforth and Crank–Nicholson methods are used for time integration. For inviscid or high Reynolds number cases, hyperviscosity, similar to the one used by Barranco and Marcus [2006], is applied to remove energy from high wavenumbers. Because rotating stratified flows support inertio–gravity waves which reflect back from the periodic boundaries, a thin Rayleigh frictional layer (sponge layer) is added at the edges of the domain to damp wave reflections.

The center of the computational domain is at $\mathbf{x} = 0$. For all cases, the background density stratification is linear $\bar{\rho}(z) = \rho_o(1 - \bar{N}^2 z/g)$ where $\bar{N}$ is constant. The suction rate function $q(\mathbf{x}, t)$ is defined as

$$q(\mathbf{x},t) = \begin{cases} q_o(\mathbf{x}) & 0 \le t/t_s \le 1 \\ q_o(\mathbf{x})\, \exp\left[-500\,(t/t_s - 1)\right] & 1 < t/t_s \le 1.05 \\ 0 & t/t_s > 1.05 \end{cases} \tag{3.17}$$

where $q_o(\mathbf{x})$ is non–zero (negative) and nearly uniform inside a spherical region of radius R centered at $\mathbf{x} = 0$ and rapidly vanishes outside of the sphere (see Appendix A for more details). The integral of $q_o(\mathbf{x})$ over the spherical region is equal to Q_o which is a given parameter. For all numerical simulations, 256^3 Fourier modes are used and $R = \pi/2$ cm and $D = 20R$, unless otherwise stated. Time steps Δt are chosen so that $f\Delta t = 0.05$ or smaller.

3.4 Relative Effect of Rotation versus Stratification

The time evolutions of super–stratification and cyclonic vorticity strongly depend on the magnitude of the horizontal divergence $\nabla_\perp \cdot \mathbf{v}_\perp$ and the vertical divergence $\partial w/\partial z$ (see equation 3.16 and sections 3.5 and 3.5). Therefore, we first study how the horizontal and vertical divergences are affected by rotation and density stratification, in particular, to understand how they change with $f/\bar{N}$.

In a non–rotating constant–density flow such as Case S1 (see Table 3.1), suction is expected to produce a flow with no directional preference (i.e., an isotropic flow). In fact, the flow in Case S1 is isotropic, and for this case $(\partial u/\partial x)_c = (\partial v/\partial y)_c = (\partial w/\partial z)_c = q_c/3$ (Figure 3.2a), where the subscript c means evaluated at $\mathbf{x} = 0$. Adding rotation or stratification breaks the symmetries of the flow. Assuming strong rotation (i.e., $f \gg |\omega_z|$), negligible viscous effects, and ignoring the fast time scales, no other term (3.16) can balance the second term on the right–hand, resulting in $|\nabla_\perp \cdot \mathbf{v}_\perp| \approx 0$. Without suction and stratification, the Taylor-Proudman theorem would follow from this analysis [Kundu and Cohen, 2010]. In the presence of suction, $|\nabla_\perp \cdot \mathbf{v}_\perp| \approx 0$ along with the continuity equation $\nabla \cdot \mathbf{v} = q$ gives $\partial w/\partial z \approx q$ (Case S2 in Figure 3.2a). Therefore, in this case the flow toward the suction region is mainly vertical.

Case	f	$\bar{N}$	Q_o	t_s	Comment	Ro	$\frac{N_c}{\bar{N}}$	$\frac{(\nabla_\perp \cdot \mathbf{v}_\perp)_c}{q_c}$
E1	1.75	1.75	-6	20				
E2	1.75	2	-0.6	45				
E3	2	1.4	-0.24	20				
E4	2	1.4	-3	15				
E5	2	1.8	-12	8				
E6	1.75	1.75	-1.2	50				
E7	1.75	2	-0.24	40				
E8	1.75	1.75	-1.2	100				
E9	1.75	1.75	-3	80				
E10	1.75	1.75	-3	40				
S1	0	0	-2	40	constant ρ	$\lvert\omega_z\rvert \approx 0$		0.67
S2	2	0	-2	40	constant ρ	0.04		0.01
S3	0	2	-2	40		$\lvert\omega_z\rvert \approx 0$	1.00	1.00
S4	5	2	-2	40		0.75	3.63	0.36
S5	2	2	-2	40		1.58	2.50	0.57
S6	10	2	-2	40		0.41	4.28	0.21
S7	5	2	-1	40		0.39	1.86	0.42
S8	5	2	-2	40	$\nu = 0$	0.84	3.26	0.11
S9	5	2	-20	40		2.96	8.35	0.03
S10	5	2	-4	20		0.8	3.87	0.21

Table 3.1: Cases in laboratory experiments (E) and numerical simulations (S). f [rad/s] and $\bar{N}$ [rad/s] are the Coriolis parameter and the Brunt–Väisälä frequency of the background density stratification, respectively. Q_o [cm^3/s] is the imposed volumetric suction rate. Suction starts at $t = 0$ and ends at t_s [s]. The working fluid in the experiments is salt–water with $\rho_o = 1.02$ g/cm^3 and $\nu = 0.01$ cm^2/s. In the simulations, $\rho_o = 1$ g/cm^3 and $\nu = 0.01$ cm^2/s, unless otherwise stated. The three columns on the right show the Rossby number Ro (defined in (3.20)), normalized Brunt–Väisälä frequency at the center of the vortex $N_c/\bar{N}$, and normalized horizontal divergence evaluated the center of the cyclone, all at the end of suction $t = t_s$.

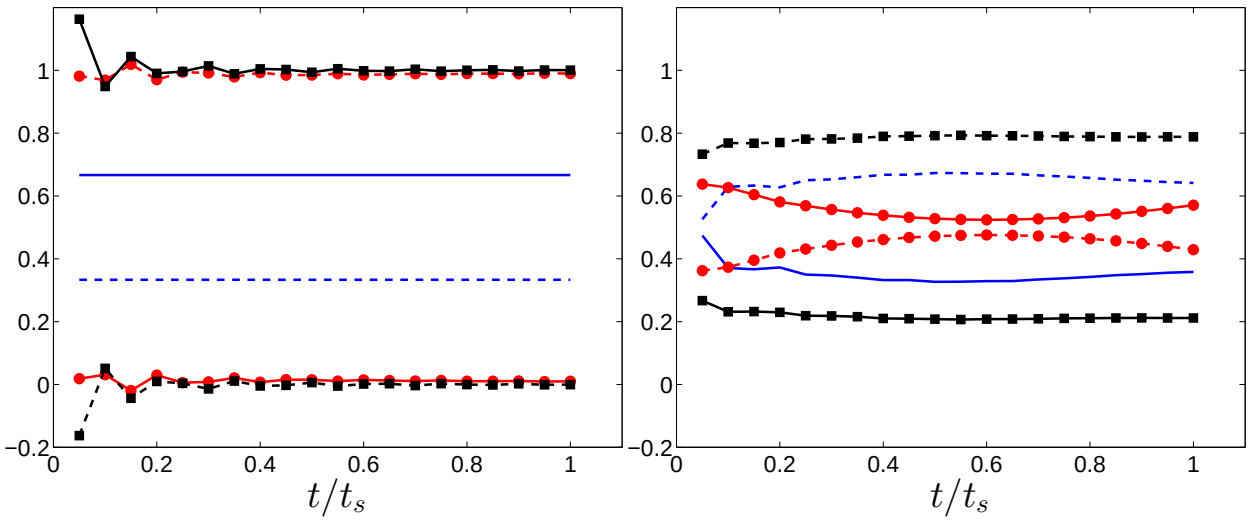

Figure 3.2: Effect of rotation and stratification on the divergence of the velocity field during suction. The solid lines show the normalized horizontal divergence $((\nabla_\perp \cdot \mathbf{v}_\perp)/q)_c$ and the broken lines show the normalized vertical divergence $((\partial w/\partial z)/q)_c$. (a) The flow in Case S1 (blue, no symbol) is non–rotating ($f = 0$) and constant–density and has $((\nabla_\perp \cdot \mathbf{v}_\perp)/q)_c = 2/3$ and $((\partial w/\partial z)/q)_c = 1/3$. The vertical divergence $\partial w/\partial z$ dominates in Cases S2 (red •) which is rotating and constant–density. The flow in Case S3 (black ■) is non–rotating ($f = 0$) and stratified, and has a dominant horizontal divergence. (b) Case S4 has $f/\bar{N} = 2.5$ (blue, no symbol), Case S5 has $f/\bar{N} = 1$ (red •), and Case S6 has $f/\bar{N} = 5$ (black ■).

Strong stratification suppresses vertical motions and decouples the flow into horizontal layers [Kundu and Cohen, 2010]. As a result, for a non–rotating stratified flow such as Case S3, we expect $\partial w/\partial z \approx 0$ and $\nabla_\perp \cdot \mathbf{v}_\perp \approx q$, which is observed in Figure 3.2a. Hence, the flow in this case approaches the suction region largely horizontally. Oscillations in Cases S2 and S3 (Figure 3.2a) are due to the inertial and internal gravity waves, respectively.

In the presence of both rotation and stratification, the relative magnitude of the horizontal and vertical divergences depends on $f/\bar{N}$. Figure 3.2b compares Cases S4–S6, which have $f/\bar{N} = 2.5$, 1, and 5, respectively. As expected, a larger $f/\bar{N}$ results in a larger vertical divergence $|\partial w/\partial z|$ compared to the horizontal divergence $|\nabla_\perp \cdot \mathbf{v}_\perp|$. This understanding of the role of $f/\bar{N}$ will be used in sections 3.5 and 3.5 and is consistent with the analytical results of McDonald [1992] for a point sink in rotating stratified flows (see his Figure 1).

3.5 Flow Field During Suction

This section focuses on the flow field during suction, i.e. $t \leq t_s$. Table 3.1 lists the experimental and numerical cases and their parameters. Note that in this paper we do not try to quantitatively compare the numerical and experimental results during and after suction because the presence of the pipe is not accounted for in the numerical solutions. Furthermore, a suction region as small as the pipe used in the experiment could not be used in the simulations due to computational limits, while a bigger pipe could not be used in the experiments because its removal at the end of suction would destroy the cyclone. However, the experimental and numerical results agree qualitatively and they are used to complement each other in order to gain a better understanding of the physics that generate the velocity field (Section 3.5), cyclonic vorticity (Section 3.5), and density super–stratification (Section 3.5). All cyclones in simulations and experiments remained axisymmetric during suction and were centered at $\mathbf{x} = 0$. Additionally, in simulation the vortices are symmetric with respect to the $z = 0$ plane (this symmetry is hard to confirm in the experiments).

Velocity Field

Figure 3.3 shows the azimuthal velocity profiles during suction for Cases E1 and E2 (as a reminder, all units are in cgs). The core in each case is in near solid–body rotation and has cyclonic vorticity. Figure 3.4 presents the evolution of the velocity field, density, and vertical vorticity during suction for Case S5. Figures 3.4a and 3.4c show the generation of radial and vertical velocities toward the suction region, and Figures 3.4b shows the development of the cyclonic azimuthal velocity. Steepening of the density profile in Figure 3.4d confirms that a super–stratified region is developed and strengthen around the suction region. Figures 3.4e and 3.4f show that a 3D cyclone is produced and intensified by suction. The vortex is found to be shielded, i.e. at each z there is a ring of weak anticyclonic vorticity around the cyclonic core (see Figures 3.4e around $x/D \approx 0.1$, see Section 3.5 for an explanation). 3D cyclones with super–stratified interior were produced in all cases in Table 3.1. The mechanisms that produce the super–stratification and cyclonic vorticity are discussed next.

Super–Stratification

As discussed in Section 3.1, the interior of a cyclone must be more stratified than the background flow (i.e., it is super–stratified). Figure 3.5 shows the evolution of $\bar{N}^2 - N^2$ during suction and after it stops for Case S4 (Note that $N \equiv \sqrt{-g(\partial\rho/\partial z)/\rho_o}$). A super-stratified region (i.e., with $\bar{N}^2 < N^2$) is created and intensified during suction (Figures 3.5a and 3.5b). Below we discuss how the density super–stratification is produced by localized suction.

Taking $\partial/\partial z$ of equation (3.9) gives

$$\frac{\partial}{\partial t}\frac{\partial \rho}{\partial z} = -(\mathbf{v}\cdot\nabla)\frac{\partial \rho}{\partial z} - \frac{\partial u}{\partial z}\frac{\partial \rho}{\partial x} - \frac{\partial v}{\partial z}\frac{\partial \rho}{\partial y} - \frac{\partial w}{\partial z}\frac{\partial \rho}{\partial z} \tag{3.18}$$

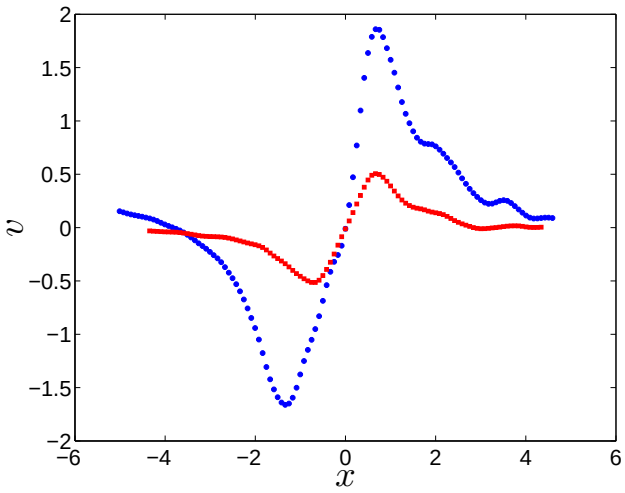

Figure 3.3: Azimuthal velocity profile along $y = z = 0$ obtained from the PIV measurements for Cases E1 (blue •) at $t/t_s = 0.15$ and E2 (red ■) at $t/t_s = 0.8$. Slope of the approximate solid–body rotation in the core Ω_c gives $Ro \equiv \Omega_c/f \approx 1$ (E1) and 0.5 (E2).

At the center (i.e., $\mathbf{x} = 0$), $\mathbf{v} = 0$ by symmetry and $\partial u/\partial z = \partial v/\partial z = 0$ (because u and v vanish along the z–axis). As a result, at the center, (3.18) reduces to

$$\frac{\partial}{\partial t} N_c^2 \;=\; -\left(\frac{\partial w}{\partial z}\right)_c N_c^2 \tag{3.19}$$

This equation shows that if $(\partial w/\partial z)_c < 0$ (which is the case for suction), the N_c increases in time from its initial value of $\bar{N}$, resulting in super–stratification (i.e., $N_c > \bar{N}$). Figure 3.6a shows the evolution of $N_c(t)$ for Cases S4, S5, and S7 during suction. Case S4 has the largest growth of N_c because it has the largest $f/\bar{N}$ and q_c, both of which create a large vertical divergence $|\partial w/\partial z|$. Case S5 has $f/\bar{N}$ smaller than Case S7, but q_c is twice as large. The net result is a faster growth of super–stratification in Case S5 compared to Case S7.

Super–stratification is also observed in the experimental results (Figure 3.6b). Case E4, which has a much stronger suction Q_o and larger $f/\bar{N}$, produces a stronger super–stratification compared to Case E5. Figure 3.7 shows $\bar{N}^2 - N^2$ in the $y = 0$ plane for Case E1 from the synthetic schlieren measurements. The pattern of the density gradient field looks qualitatively the same as the one obtained numerically (compare with Figure 3.5); however, the magnitude of super–stratification is smaller in the experiments (Figure 3.6) which is likely due to the presence of the real pipe in the experiments (also see Section 3.5).

The super–stratification decays after the suction stops in both simulations (Figures 3.5c and 3.5d) and experiments (Figure 3.7c and 3.7d). This is because, as discussed in Section 3.6, the vertical velocity changes direction once the suction stops. As a result, $\partial w/\partial z$ becomes positive, decreasing N_c and de–stratifying the flow.

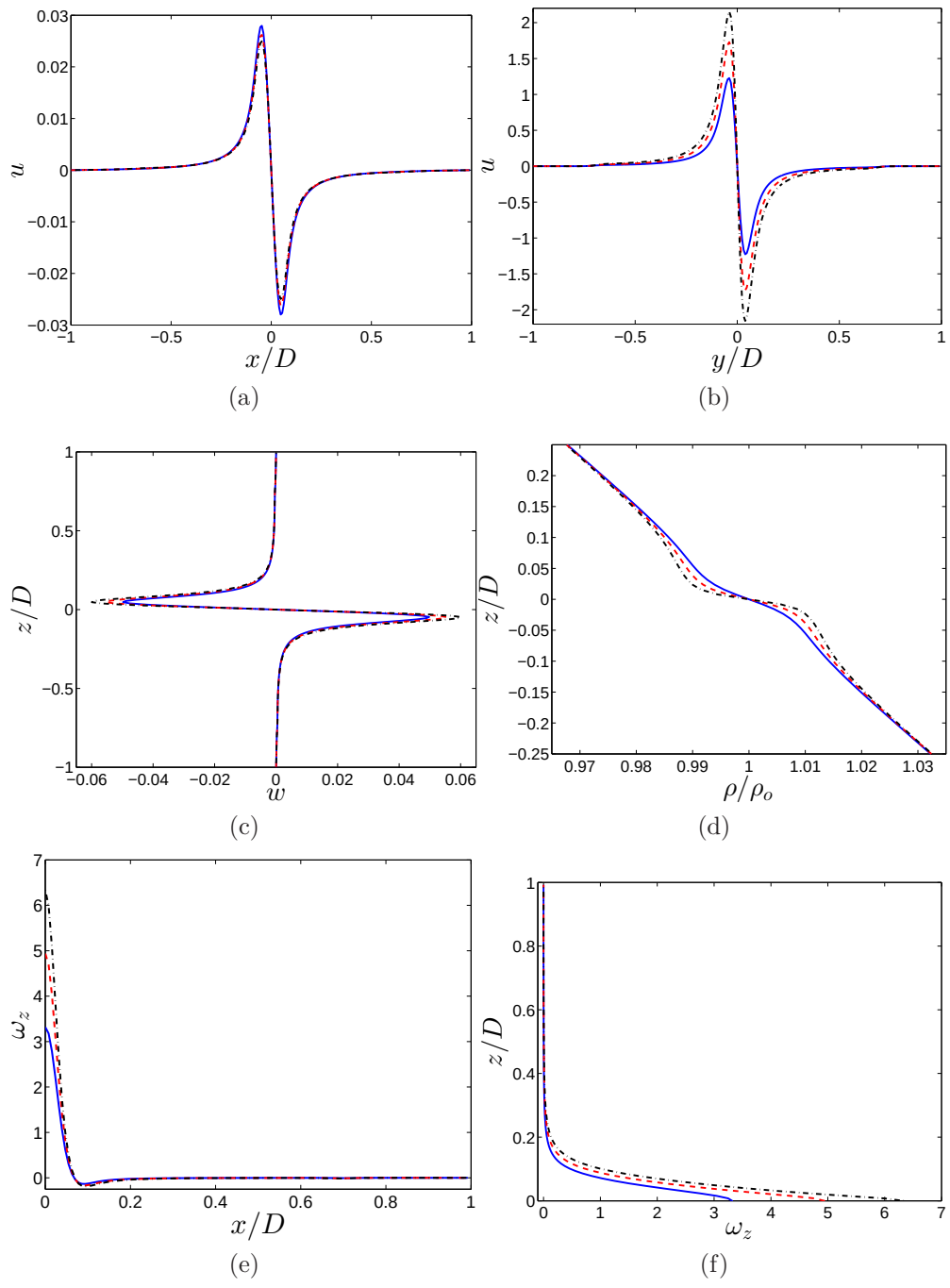

Figure 3.4: Flow field for Case S5 at $t/t_s = 1/3$ (blue solid line), $t/t_s = 2/3$ (red broken line), and $t/t_s = 1$ (black dot–dashed line). (a) Radial velocity, u along $y = z = 0$; (b) Azimuthal velocity, u along $x = z = 0$; (c) Vertical velocity, w along $x = y = 0$; (d) Density, ρ along $x = y = 0$; (e) Vertical vorticity, ω_z along $x = z = 0$; (f) Vertical vorticity, ω_z along $x = y = 0$. The flow remains axisymmetric during suction, and is symmetric with respect to the midplane $z = 0$. Only a part of the domain is shown in (d)–(f) for better illustration.

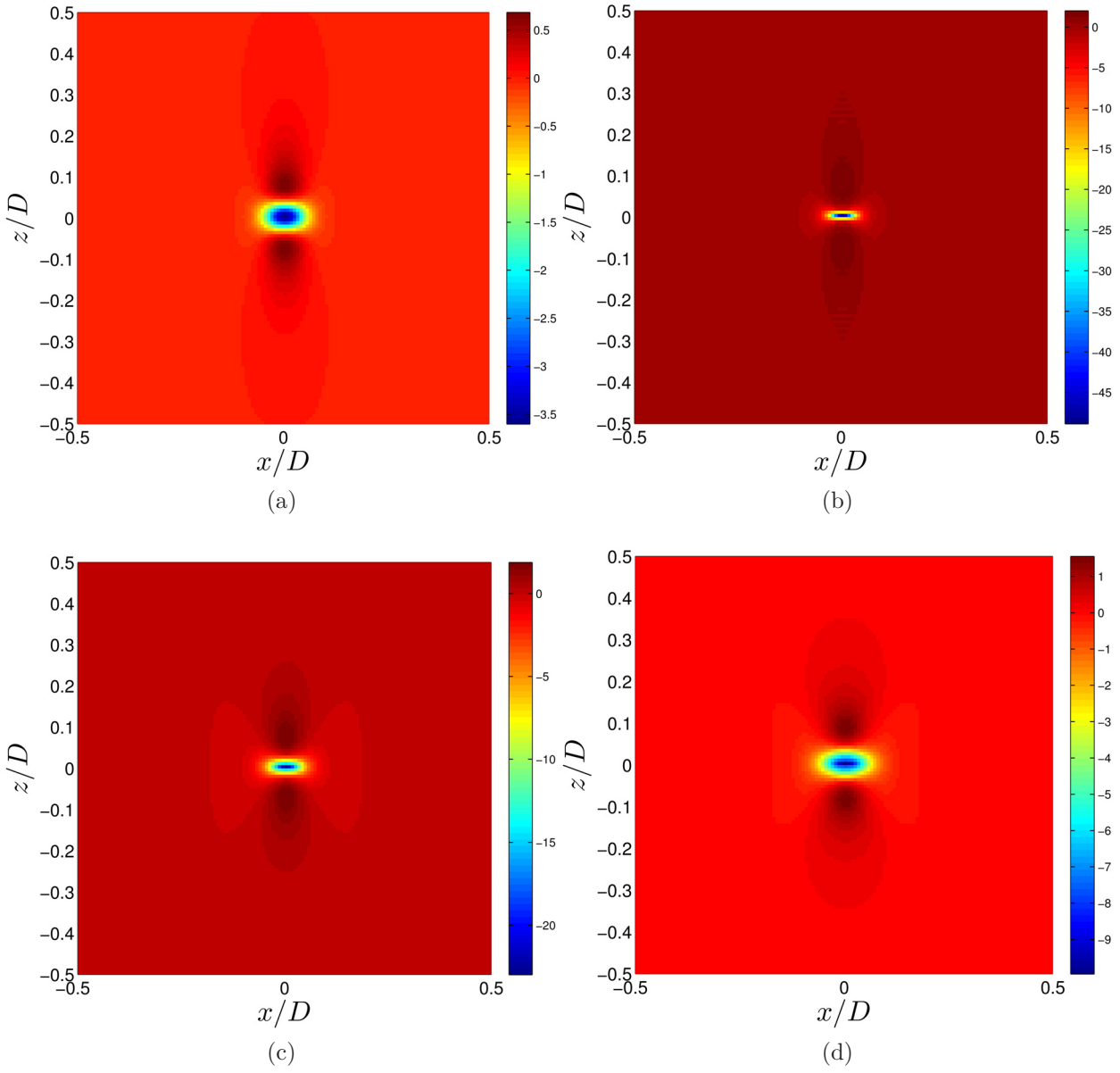

Figure 3.5: Evolution of $\bar{N}^2 - N^2 = (g/\rho_o)(\partial\tilde{\rho}/\partial z)$ in the $y = 0$ plane in Case S4 at (a) $t/t_s = 0.25$, (b) $t/t_s = 1$, (c) $t/t_s = 2$, and (d) $t/t_s = 3.75$. Only a part of the domain is shown for better illustration.

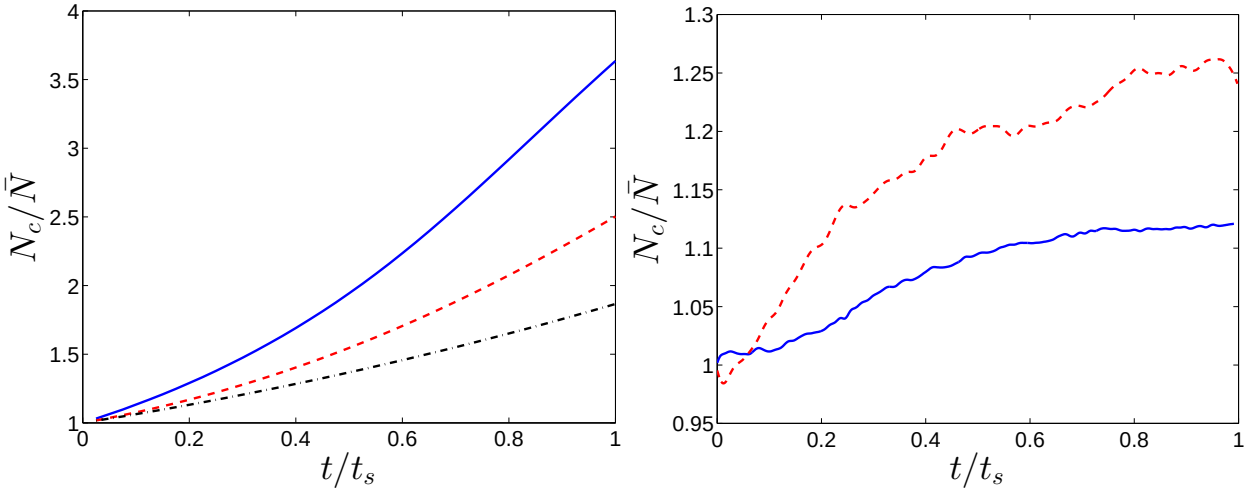

Figure 3.6: Evolution of N_c during suction in the simulations (a) and experiments (b). (a) Cases S4 (blue solid line), S5 (red broken line), and S7 (black dot–dashed line). (b) Cases E4 (blue solid line) and E5 (red broken line). See Table 3.1 for parameters of each case.

Generation of Cyclonic Vorticity

In cases with rotation, vertical vorticity ω_z is produced in the flow in both simulations and experiments. We define the Rossby number Ro as the ratio of the angular velocity at the vortex core to the Coriolis parameter, which in the numerical cases can be calculated as

$$Ro \equiv \frac{\omega_c}{2f}, \tag{3.20}$$

where ω_c is the vertical vorticity at the vortex center. Figure 3.8a shows the evolution of the Rossby number of the cyclones during suction for Cases S4, S5, and S7, which have different $f/\bar{N}$ and Q_o (see Table 3.1). To better understand the generation of cyclonic vorticity and the effect of these parameters on the magnitude of Ro, we look at equation (3.16). As a result of the symmetries mentioned before, $\mathbf{v} = 0$ at $\mathbf{x} = 0$ and $w = 0$ in the $z = 0$ plane. Therefore, at $\mathbf{x} = 0$ equation (3.16) simplifies to

$$\frac{\partial \omega_c}{\partial t} = -\omega_c(\nabla_\perp \cdot \mathbf{v}_\perp)_c - f(\nabla_\perp \cdot \mathbf{v}_\perp)_c + \nu(\nabla^2 \omega_z)_c \tag{3.21}$$

In this equation, only the second term on the right–hand side can produce vorticity if $\boldsymbol{\omega} = 0$ initially. Figure 3.8b shows the evolution of each term of this equation for Case S4. At the beginning, cyclonic vorticity is produced and intensified by the effect of the background rotation (i.e., the $f(\nabla_\perp \cdot \mathbf{v}_\perp)_c$ term). Once ω_c becomes comparable to f, the first term on the right–hand side becomes significant as well, but so does the viscous term. These two

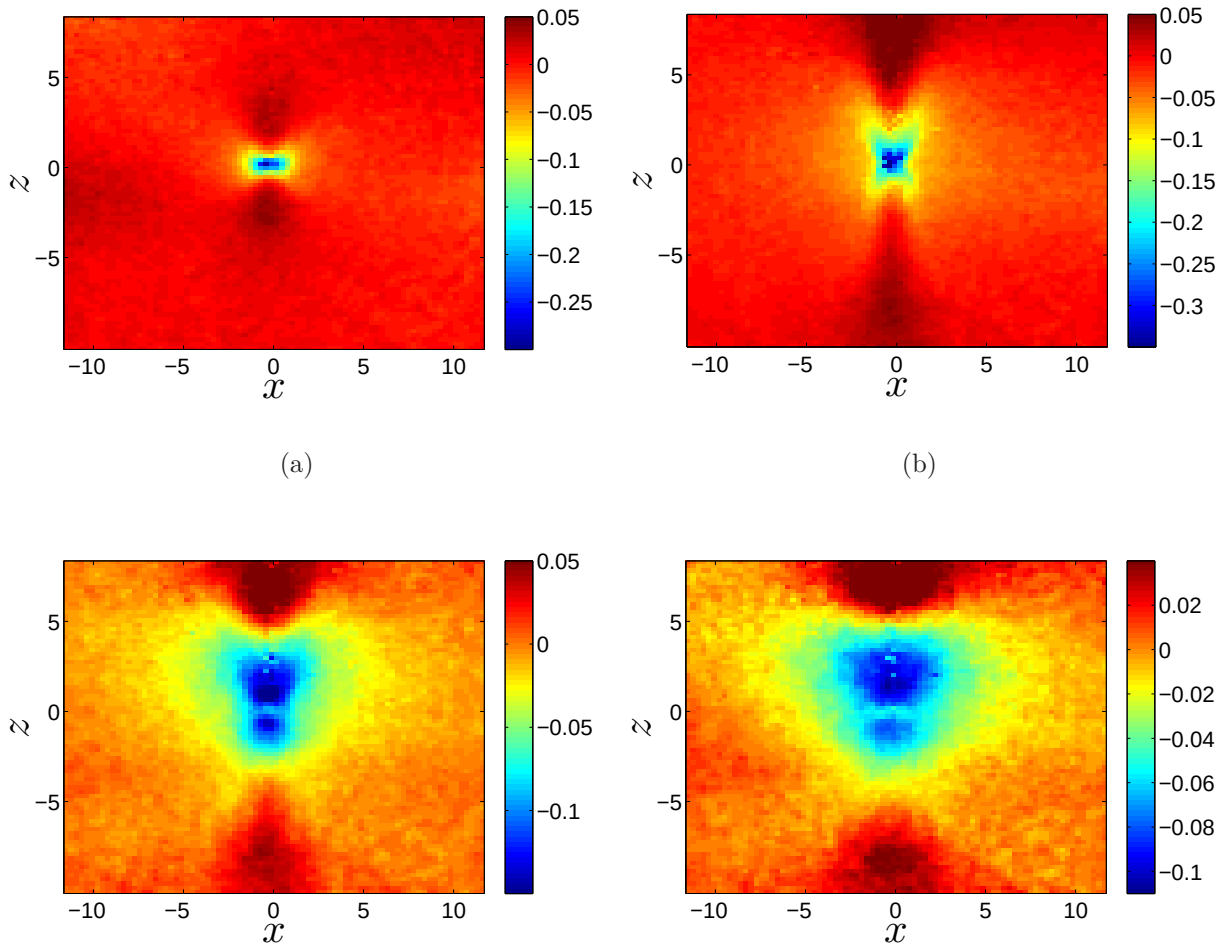

(a) (b)

(c) (d)

Figure 3.7: Evolution of $\bar{N}^2 - N^2 = (g/\rho_o)(\partial\tilde{\rho}/\partial z)$ in the $y = 0$ plane in Case E1 visualized by the synthetic schlieren technique at (a) $t/t_s = 0.25$, (b) $t/t_s = 1$, (c) $t/t_s = 2$, and (d) $t/t_s = 3.75$.

terms, which both depend on the magnitude of ω_c, nearly counter balance each other. The net result is a gradual decrease of $\partial\omega_c/\partial t$ over time. This can stop the growth of Ro in more viscous cases, in particular in the presence of a real pipe in the experiments. The other numerical cases in Table 3.1 follow the same mechanism as S4 in producing cyclones.

Generation of the anticyclonic shield around the cyclonic core (see Figure 3.4e) is due to the change in the sign of the horizontal divergence outside the core (see Figure 3.4a). The positive horizontal divergence outside the core produces anticyclonic vorticity through the $-f(\nabla_\perp \cdot \mathbf{v}_\perp) < 0$ term in equation 3.16. The magnitude of $|\omega_z|$ in the shield is much weaker than the magnitude of $|\omega_z|$ in the core; this is because, in (3.16), not only $|\nabla_\perp \cdot \mathbf{v}_\perp|$ is smaller in the shield, but also $(f + \omega_z) > f$ $(< f)$ if $f\omega_z > 0$ (< 0).

To understand the effect of $f/\bar{N}$ and $q_c/\bar{N}$ on Ro, equation (3.21) is rewritten as

$$\frac{\partial Ro}{\partial t} = -(0.5 + Ro)(\nabla_\perp \cdot \mathbf{v}_\perp)_c + \nu\frac{(\nabla^2\omega_z)_c}{2f} \tag{3.22}$$

In this equation, the difference between Cases S4 and S5 is the magnitude of the horizontal divergence which is larger in Case S5 (because it has a smaller $f/\bar{N}$). As a result, the second term on the right–hand side is larger in magnitude in Case S5, resulting in a larger $\partial Ro/\partial t$ and therefore larger growth of Ro (see Figure 3.8a). Suction in Case S7 is weaker compared to Case S4 (i.e., smaller $|q_c|/\bar{N}$). This results in a smaller horizontal divergence in Case S7 (compared to S4), and finally a weaker cyclone. Notice that no vorticity is produced in a non–rotating constant–density flow because if $f = 0$ and $\nabla\tilde{\rho} = 0$, there is no term in equation (3.15) that can produce vorticity if $\mathbf{v} = \boldsymbol{\omega} = 0$ initially (see Table 3.1).

Figure 3.9 shows the evolution of the Rossby number Ro in Cases E2, E6, and E7. Using the PIV measurements, the angular velocity used in the calculation of the Rossby number is extracted from the approximate solid–body rotation at the core of the cyclone. As expected, increasing the suction rate Q_o (with $f/\bar{N}$ kept roughly the same) results in larger Ro. In cases with stronger suction (i.e., larger $Q_o t_s$), such as Cases E8 and E9, the growth of the Rossby number is observed to stop around $Ro = 1$ which might be due to large viscous dissipation around the pipe.

3.6 Flow Field After Suction Stops

After the suction stops, the cyclones decay in simulations (Figure 3.10a) and in experiments (Figure 3.10b) because of viscous dissipation. Figure 3.11 shows the azimuthal velocity field after the suction stops for Cases E1 and E2. In each case, the core is nearly in solid–body rotation, but the angular velocity has reduced after the suction stopped (compare with Figure 3.3). Figure 3.12 shows the flow field (velocity, density, and vorticity) of Case S4 at three different times after the suction stops. The radial and azimuthal velocities and vertical vorticity decrease in time due to the viscous dissipation, and the density anomaly $\tilde{\rho} = \rho - \bar{\rho}$ reduces, weakening the super–stratification. The reduction of super–stratification is due to the reversal of the direction of the vertical velocity after the suction stops (compare

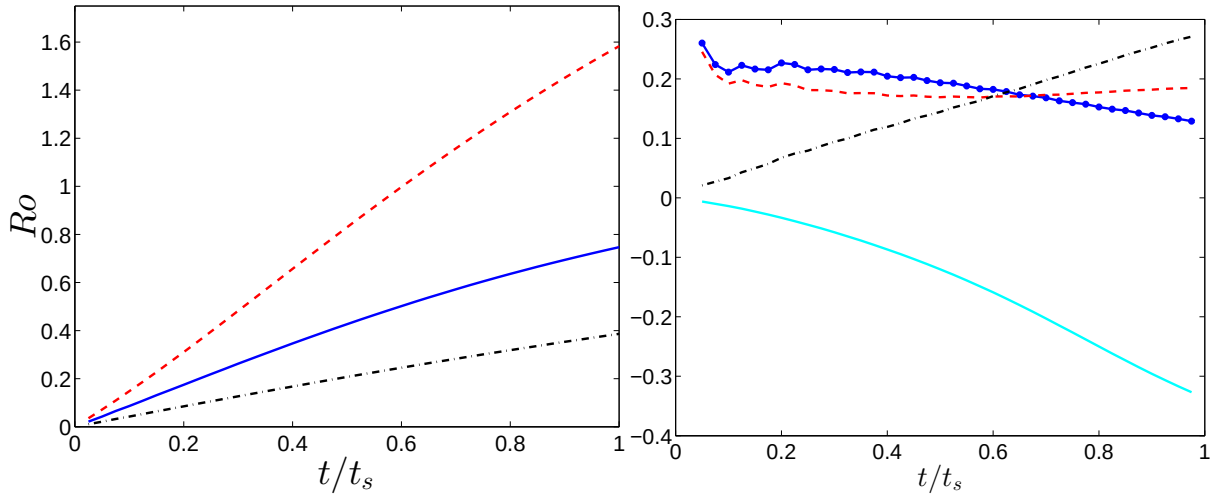

Figure 3.8: (a) Evolution of the Rossby number $Ro \equiv \omega_c/(2f)$ for Cases S4 (blue solid line), S5 (red broken line), and S7 (black dot–dashed line), where ω_c is the the vertical vorticity at the center of the vortex. (b) Case S4, evolution of different terms of equation (3.21) at $\mathbf{x} = 0$: $(\partial\omega_c/\partial t)$ (blue marked line), $-f(\nabla_\perp \cdot \mathbf{v}_\perp)_c$ (red broken line), $-\omega_c(\nabla_\perp \cdot \mathbf{v}_\perp)_c$ (black dot–dashed line), and $\nu(\nabla^2\omega_z)_c$ (light blue solid line).

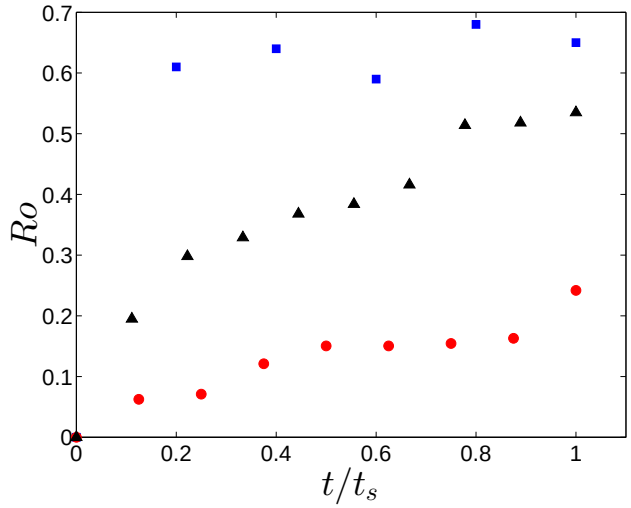

Figure 3.9: Evolution of Ro during suction in the experiments for Cases E2 (black ▲), E6 (blue ■) and E7 (red •). Cases E2, E6, E7 have $(f/\bar{N}, Q_o) = (0.875, -0.6)$, $(1, -1.2)$, $(0.875, -0.24)$, respectively (see Table 3.1).

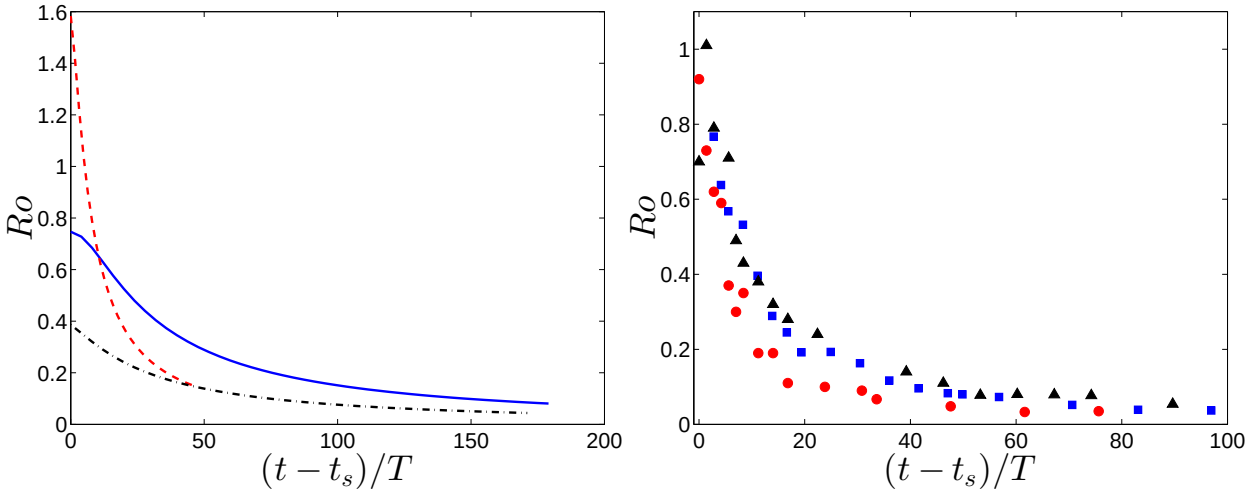

Figure 3.10: Evolution of Ro in simulations (a) and experiments (b) after suction stops for Cases (a) S4 (blue solid line), S5 (red broken line), and S7 (black dot–dashed line); (b) E6 (red •), E8 (blue ■), and E9 (black ▲). See Table 3.1 for the parameters of each case. $T = 4\pi/f$ is the inertial period.

Figures 3.4c and 3.12c). The physics behind this reversal and its consequences are discussed below.

Secondary Circulation

Viscous dissipation induces a meridional secondary circulation in decaying cyclones and anticyclones [Hassanzadeh et al., 2012]. This ageostrophic flow consists of vertical and radial velocities and can be explained by looking at the dominant horizontal force balance of the vortex. As discussed before, cyclones in cyclo–geostrophic balance have low–pressure centers, so that in a horizontal plane, the inward pressure force balances the outward Coriolis and centrifugal forces, which are both proportional to the azimuthal velocity. Viscous dissipation reduces the azimuthal velocity (and consequently the Coriolis and centrifugal forces), resulting in an imbalance between the inward and outward horizontal forces. As a result, a radial flow is induced toward the low–pressure center. A converging radial flow (i.e., negative horizontal divergence) produces a positive vertical divergence (i.e., $\partial w/\partial z > 0$) due to conservation of mass (notice that $q = 0$ now). Therefore, the direction of the radial flow in a viscously decaying cyclone (Figure 3.12a) is the same as the direction of the radial flow during suction (Figure 3.4a); on the other hand, the direction of the vertical velocity flips (see Figures 3.4c and 3.12c). Reversal of the vertical velocity (and the change in the sign of the vertical divergence) occurs quickly in all numerical cases in Table 3.1 (see Figure 3.13), except for Case S8 (inviscid) in which the vertical and radial velocities rapidly disappear. In-

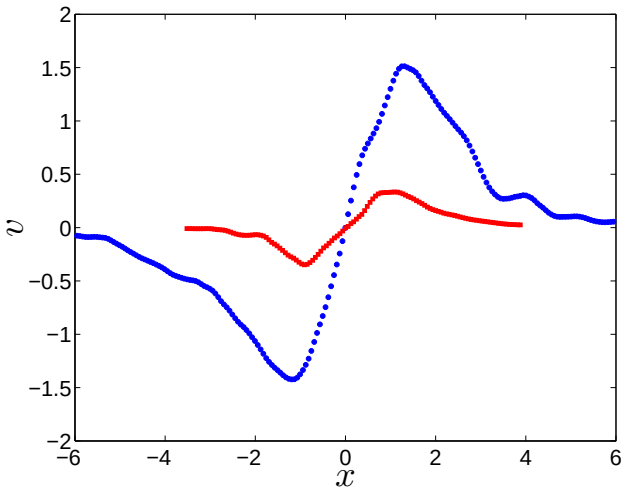

Figure 3.11: Azimuthal velocity profile obtained from the PIV measurements for Cases E1 (blue •) at $(t - t_s)/T = 3.5$ and E2 (red ■) at $(t - t_s)/T = 12$. Slope of the approximate solid–body rotation in the core gives $Ro \approx 0.9$ (E1) and $Ro \approx 0.24$ (E2).

terestingly, this abrupt change in the ageostrophic flow does not de–stabilize the geostrophic flow. Notice that the secondary circulations in these simulations and experiments are *not* relevant to Ekman pumping [Pedlosky, 1990] because no Ekman layer exists in our simulations (the domain is periodic), and the tall layer of stratified fluid between two the thick layers of constant density fluid (see Figure 3.1) strongly damps Ekman pumping in the experiments.

Figure 3.14a shows the streamlines of the secondary flow for Case S4 at two different times. The secondary flow extends well beyond the boundaries of the vortex (Figure 3.14b). As a result, even though the secondary flow is weak compared to the primary flow (compare Figures 3.12a and 3.12b), it plays an important role in the dynamics of the cyclone by changing its interior stratification. After the vertical velocity reverses, the positive vertical divergence reduces the super–stratification as expected from equation (3.19). Weakening of the super–stratification is observed in both numerical and experimental results (Figure 3.15, also Figures 3.5 and 3.7). Note that after the suction stopped, the conductivity probe was removed with the pipe because it was strongly disturbing the flow. Therefore $N_c(t)$ in Figure 3.7 is obtained from the synthetic schlieren measurements. Direct measurement of the weak secondary flow is a challenging task in laboratory experiments, but the reduction of $N_c(t)$ in experimental results is an indirect indication of the direction of the vertical velocity w (employing equation (3.19)). Weak secondary flows not only significantly change the interior stratification of vortices (both cyclones and anticyclones), but they can also transport tracers vertically which is of great importance in the ocean [Klein and Lapeyre, 2009] and atmosphere [de Pater et al., 2010].

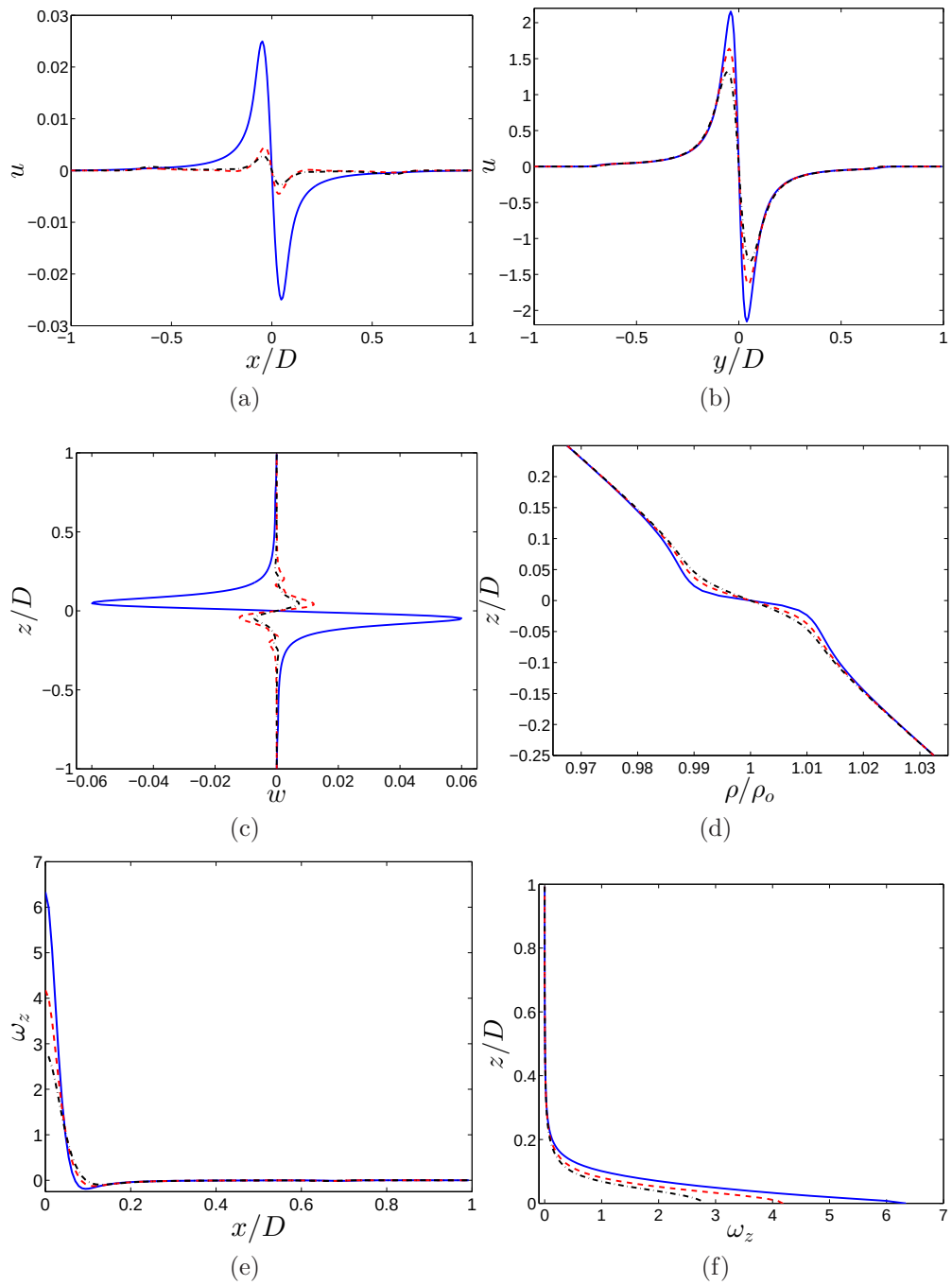

Figure 3.12: Flow field for Case S5 at $(t - t_s)/T = 0$ (blue solid line), $(t - t_s)/T = 4.8$ (red broken line), and $(t - t_s)/T = 9.6$ (black dot–dashed line). $T = 4\pi/f$ is the inertial period. (a) Radial velocity, u along $y = z = 0$; (b) Azimuthal velocity, u along $x = z = 0$; (c) Vertical velocity, w along $x = y = 0$; (d) Density, ρ along $x = y = 0$; (e) Vertical vorticity, ω_z along $x = z = 0$; (f) Vertical vorticity, ω_z along $x = y = 0$. The flow is axisymmetric, and is symmetric with respect to the midplane $z = 0$. Only a part of the domain is shown in (d)–(e) for better illustration.

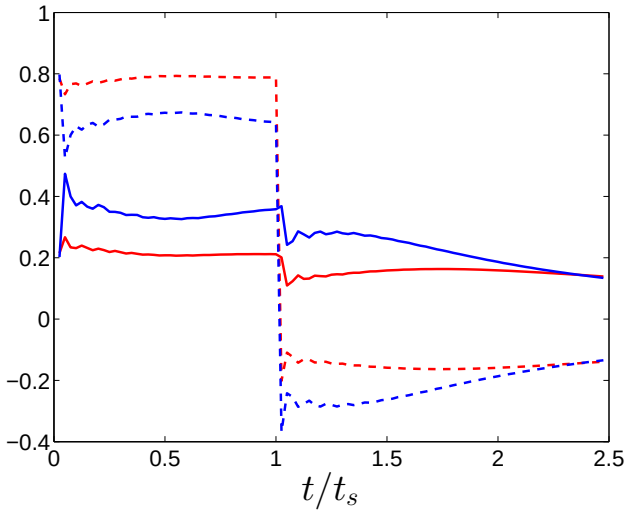

Figure 3.13: Normalized horizontal $((\nabla_\perp \cdot \mathbf{v}_\perp)/q)_c$ (solid lines) and vertical $((\partial w/\partial z)/q)_c$ (broken lines) divergences for Cases S4 (thick blue) and S6 (thin red).

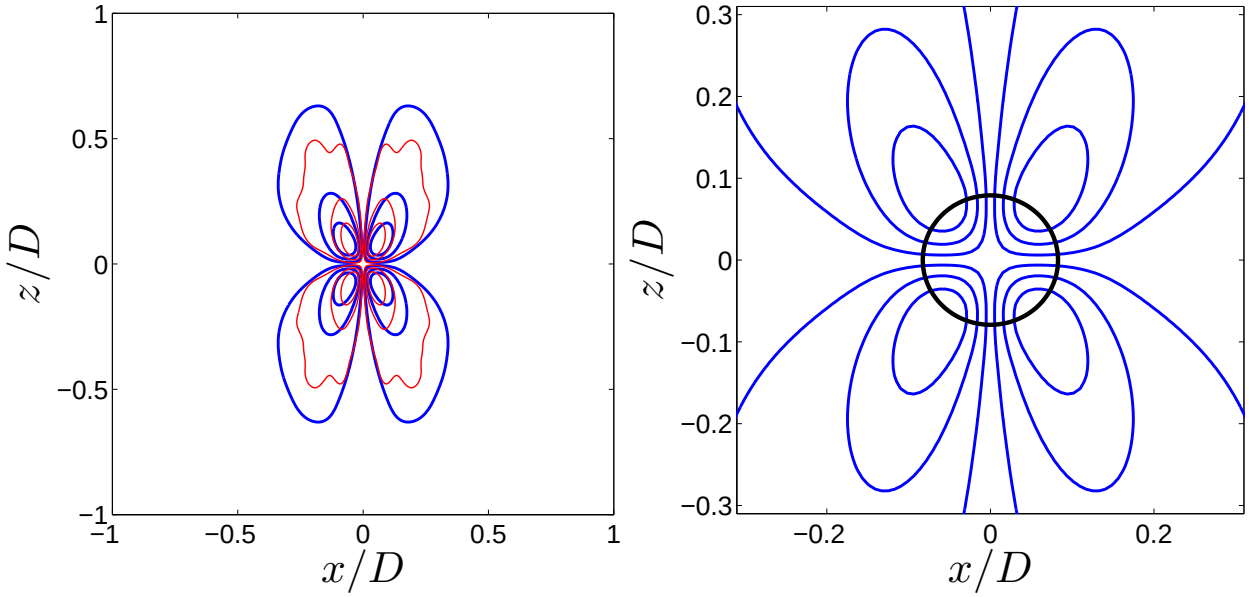

(a) (b)

Figure 3.14: Streamlines of the secondary flow for Case S4 in the $y = 0$ plane. (a) At $(t-t_s)/T = 24$ (thin red line) and $(t-t_s)/T = 103.5$ (thick blue line), $T = 4\pi/f$ is the inertial period. (b) Zoomed in at $(t - t_s)/T = 103.5$, the thick black line shows the approximate boundaries of the vortex calculated using the horizontal and vertical characteristic length scales of pressure anomaly $\tilde{p}$, see (3.24).

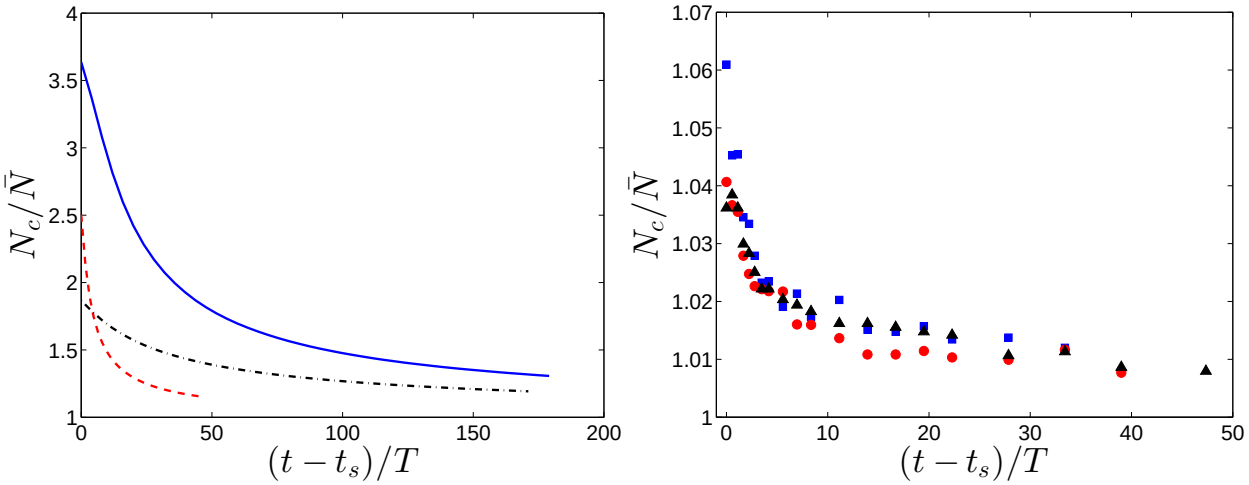

Figure 3.15: Evolution of N_c in experiments and simulations after suction stops for Cases (a) S4 (blue solid line), S5 (red broken line), and S7 (black dot–dashed line); (b) E1 (blue ■), E8 (black ▲) and E10 (red •). See Table 3.1 for the parameters of each case. $T = 4\pi/f$ is the inertial period.

Aspect Ratio

Recently, we proposed a relationship for the aspect ratio α of baroclinic vortices [Hassanzadeh et al., 2012]:

$$\left(\frac{H}{L}\right)^2 = \frac{Ro\ (1+Ro)}{N_c^2 - \bar{N}^2} f^2 \tag{3.23}$$

where H and L are the characteristic vertical and horizontal length scales of the pressure anomaly $\tilde{p}$ [see Hassanzadeh et al., 2012, for more details]. One immediate consequence of equation (3.23) is that for anticyclones (i.e., $Ro < 0$), $N_c < \bar{N}$ if $Ro > -1$, and $N_c > \bar{N}$ if $Ro < -1$, all because the right–hand side of (3.23) has to be positive. For cyclones (i.e., $Ro > 0$), this results in $N_c < \bar{N}$ for any Ro, meaning that the flow inside the cyclone has to be super–stratified.

Aubert et al. [2012] experimentally validated (3.23) for anticyclones produced by injection, and Hassanzadeh et al. [2012] confirmed this equation numerically for cyclones and anticyclones created and dissipated via various mechanisms, including two cases of cyclones produced by localized suction. Here we confirm (3.23) for more cases. Following Hassanzadeh et al. [2012], we calculate $H(t)$ and $L(t)$ as

$$H(t) = \sqrt{\left|\frac{\tilde{p}}{\partial^2\tilde{p}/\partial z^2}\right|_c} \quad \text{and} \quad L(t) = \sqrt{\left|\frac{2\tilde{p}}{\nabla_\perp^2\tilde{p}}\right|_c}, \tag{3.24}$$

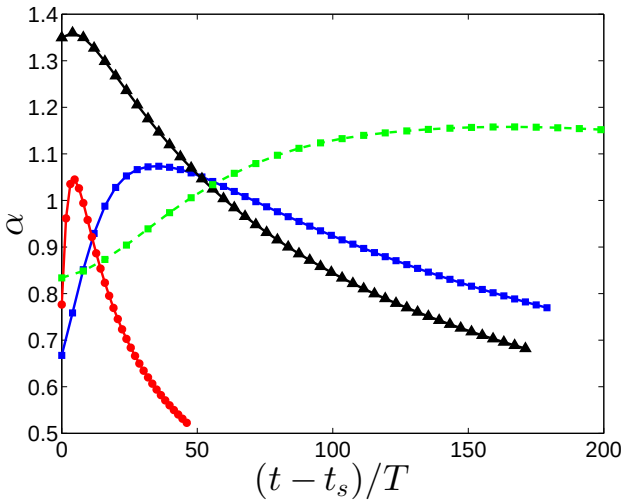

Figure 3.16: Evolution of aspect ratio calculated from (3.24) (lines) and (3.23) (symbols) for Cases S4 (blue ■), S5 (red •), S6 (black ▲), and S7 (green ■ with broken line).

and compare H/L with the aspect ratio obtained from equation (3.23) for numerically–calculated values of $Ro(t)$ and $N_c(t)$. Figure 3.16 shows how well the two aspect ratios agree. The maximum relative error is 0.3%. Accurate measurement of the aspect ratio of the cyclones, their N_c, and Ro at the same time is not feasible in the current laboratory setup; therefore, equation (3.23) could not be validated in the experiments results.

3.7 Conclusion

Creation of 3D baroclinic cyclones using localized suction in rotating linearly stratified flows is studied numerically and experimentally. Nonlinear Boussinesq equations are modified to account for localized suction, which is modeled as a small spherical sink, and the equations are solved numerically. Experiment is conducted in a rotating tank filled with salt–water, where fluid is sucked through a small pipe.

The simulations show that localized suction produces negative vertical $\partial w/\partial z < 0$ and horizontal $\nabla_\perp \cdot \mathbf{v}_\perp < 0$ divergences, and that the relative strength of the divergences depends on the ratio of the Coriolis parameter to the Brunt–Väisälä frequency $f/\bar{N}$. The vorticity (3.21) and density (3.19) equations simplified using the symmetries of the flow show that negative horizontal divergence produces cyclonic vorticity, and that negative vertical divergence creates local super–stratification. In each experimental and numerical case (except the non–rotating and constant–density ones), a single coherent long–lived 3D cyclone with a super–stratified interior is created and intensified during suction. Super–stratification is visualized in the experiments using the synthetic schlieren technique.

Once the suction stops, the cyclones decay due to the viscous dissipation. A simple

physical argument is given on why a viscously decaying cyclone has a secondary circulation (i.e., non–zero vertical and radial velocity) with $\partial w/\partial z > 0$ and $\nabla_\perp \cdot \mathbf{v}_\perp < 0$. Therefore, the vertical velocity is expected to reverse once the cyclone starts to decay. The reversal is observed in the numerical results. Although the secondary circulation is much weaker than the cyclo–geostrophic flow, its role in the dynamics of the cyclone is significant. The vertical velocity with positive divergence mixes the flow inside and outside of the cyclone and reduces the super—stratification (as evident from (3.19)). Measuring the secondary flow is challenging in the laboratory, but the weakening of the super–stratification in the experimental results is an indirect evidence of the reversal of the vertical velocity.

This paper provides a better understanding of the physics of the flows produced by localized suction in rotating stratified flows, the mechanisms that create cyclonic vorticity and local super–stratification, and the secondary circulation of viscously decaying 3D baroclinic cyclones. This understanding can be applied later to design and conduct well–controlled experimental studies of cyclone–anticyclone asymmetry, and in particular the implications of this asymmetry for the stability, longevity, and secondary circulation of geophysical and astrophysical vortices. In addition, the role of the secondary circulation in the dynamics of 3D vortices, especially its effect on their internal stratification and longevity, merits further numerical and experimental investigation.

Chapter 4

Self–Replicating 3D Vortices in Stably–Stratified Rotating Shear

4.1 Introduction

For a protostar to accrete gas from its surrounding protoplanetary disk (PPD) [Armitage, 2011] and grow into a star, the PPD must have an instability capable of transporting angular momentum radially outward [Balbus and Hawley, 1998]. This requirement has led to an intense effort to find instabilities in PPDs and other rotating flows in which the angular momentum satisfies Rayleigh's criterion for centrifugal stability, i.e., the absolute value of the angular momentum increases with increasing radius [Rayleigh, 1917]. Numerical studies [Balbus et al., 1996, Shen et al., 2006] of ideal gases in PPDs and experimental studies [Ji et al., 2006] of constant density fluids in rotating flows where the velocity obeys Rayleigh's criterion show that the flows are both linearly and finite-amplitude stable to hydrodynamic perturbations. In regions of a PPD where the gas is sufficiently ionized to couple to magnetic fields, the magneto-rotational instability (MRI) [Balbus and Hawley, 1998] can operate. However, large regions of PPDs, known as *dead zones*, are too cool to ionize sufficiently and have MRI. Strato-rotational instabilities [Le Bars and Le Gal, 2007] and Rossby wave instabilities [Lovelace et al., 1999] could de-stabilize a PPD, but they require unrealistic impermeable radial boundaries on the PPD or a large continually-forced density perturbation, respectively. Thus, star formation remains problematic.

Here we report a new type of finite-amplitude instability that occurs in neutrally-stable, shearing flows with stably-stratified densities (as in a PPD) and with velocities that would satisfy Rayleigh's stability criterion if the densities were constant – as assumed in Rayleigh's

With minor modifications, Chapter 3 appears in:
P. S. Marcus, S. Pei, C–H Jiang, and P. Hassanzadeh, *Self–Replicating Three–Dimensional Vortices in Neutrally-Stable Stratified Rotating Shear Flows*, submitted to the Physical Review Letters, 2013.

analysis. These flows include plane and circular Couette flows, which have been used to model PPDs. Our new instability allows a small-size perturbation to form large vortices. In particular, their radii can be as large as the vertical pressure scale height of a PPD. The 3D vortices found in our study have a unique property: a vortex that grows from a single, local perturbation triggers a 1^{st}-generation of vortices that grow at nearby locations. The 1^{st}-generation of vortices grows large and triggers a 2^{nd}-generation. The triggering of subsequent generations continues *ad infinitum*. The vortices do not advect in the cross-stream direction (radial direction of a PPD), but the front dividing the vortex-populated fluid from the unperturbed fluid does. This is shown in Figures 4.1 and 4.2. Because the vortices grow large and spawn new generations of vortices that march across the domain of a *dead* zone, we refer to vortices that *self-replicate* in this manner as *zombie vortices*. To understand star formation, it is important to determine how initial noise creates instabilities, but here we focus on the formation and self-replication of zombie vortices.

The simplest flow that is not linearly unstable in which zombie vortices occur is a vertically stably-stratified Boussinesq fluid in an unbounded plane Couette flow. The unperturbed velocity is

$$\mathbf{v} = \bar{V}(x)\ \hat{\mathbf{y}} \tag{4.1}$$

with

$$\bar{V}(x) \equiv \sigma x, \tag{4.2}$$

where σ is the uniform shear, x and y are the cross-stream and stream-wise coordinates respectively, and quantities with "hats" are unit vectors. The span–wise direction is z, which is also the direction of density stratification and gravity g, so that the unperturbed density is

$$\bar{\rho}(z) = \rho_0(1 - N^2 z/g), \tag{4.3}$$

where ρ_0 is a constant and

$$N \equiv \sqrt{-\frac{g}{\rho_0}\frac{d\bar{\rho}}{dz}} \tag{4.4}$$

is the Brunt-Väisälä frequency, which is uniform throughout the domain. The flow is on a rotating turntable with angular velocity $\Omega\hat{\mathbf{z}} \equiv f/2\hat{\mathbf{z}}$, where f is the Coriolis parameter.

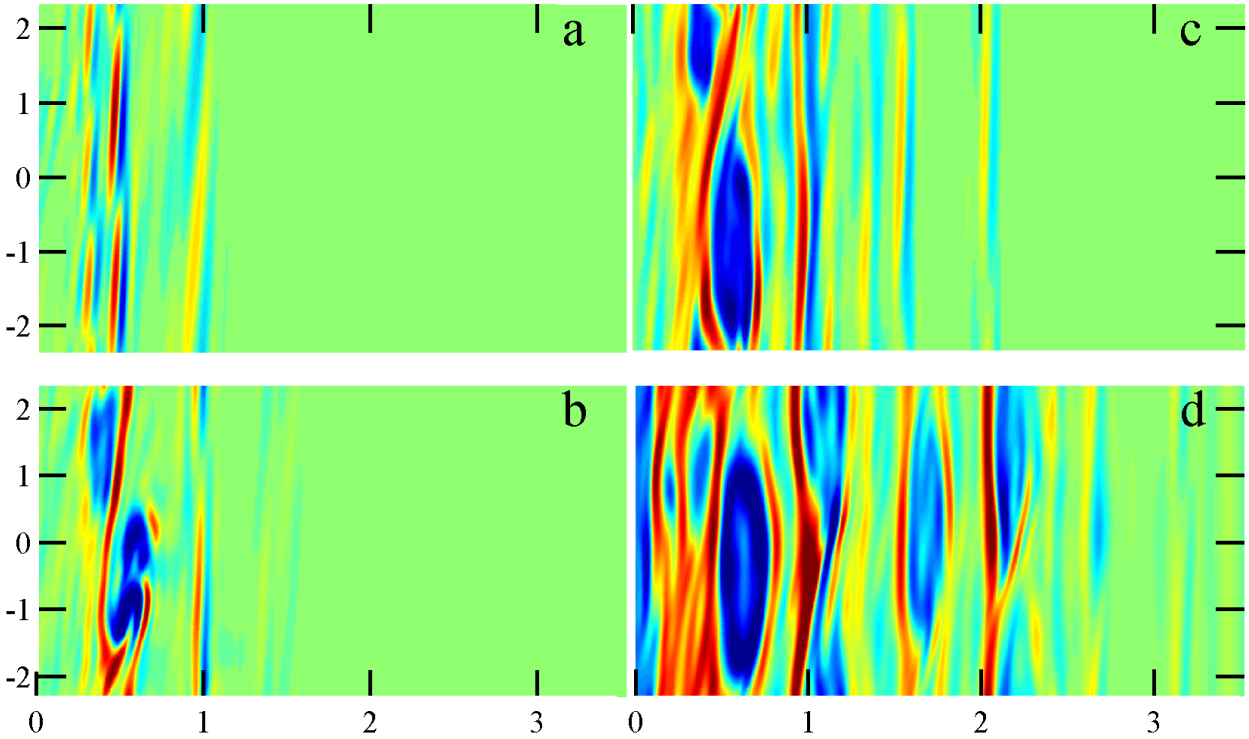

Figure 4.1: Zombie vortices start near the origin in the x–y plane with subsequent generations sweeping outward in x (the horizontal axis is x, the vertical axis is y). The vorticity ω_z is red for cyclones; blue for anticyclones; and green for $\omega_z = 0$. This Couette flow has $f/N = 1$ and $\sigma/N = -3/4$. The perturbing vortex at the origin cannot be seen because the plane shown here is at $z = -0.404$. The x-y computational domain is $|x| \le 4.7124$; $|y| \le 2.3562$, and is larger than shown. (a) $t = 64/N$. (b) $t = 256/N$. (c) $t = 576/N$. (d) $t = 2240/N$. See text for details.

4.2 Critical Layers

In the rotating frame, the dissipationless equations for the velocity $\mathbf{v}$ are:

$$\frac{\partial \mathbf{v}}{\partial t} = -(\mathbf{v}\cdot\nabla)\mathbf{v} - \frac{\nabla\Pi}{\rho_0} + f\mathbf{v}\times\hat{\mathbf{z}} - \frac{(\rho-\rho_0)g}{\rho_0}\hat{\mathbf{z}} \tag{4.5}$$

$$\frac{\partial \rho}{\partial t} = -(\mathbf{v}\cdot\nabla)\rho \tag{4.6}$$

$$\nabla\cdot\mathbf{v} = 0, \tag{4.7}$$

where Π is the pressure head. When equations (4.5)–(4.7) are linearized about $\bar{\mathbf{v}} = \bar{V}(x)\,\hat{\mathbf{y}}$ and $\bar{\rho}(z)$, the eigenmodes are proportional to

$$e^{i(k_y y + k_z z - st)},$$

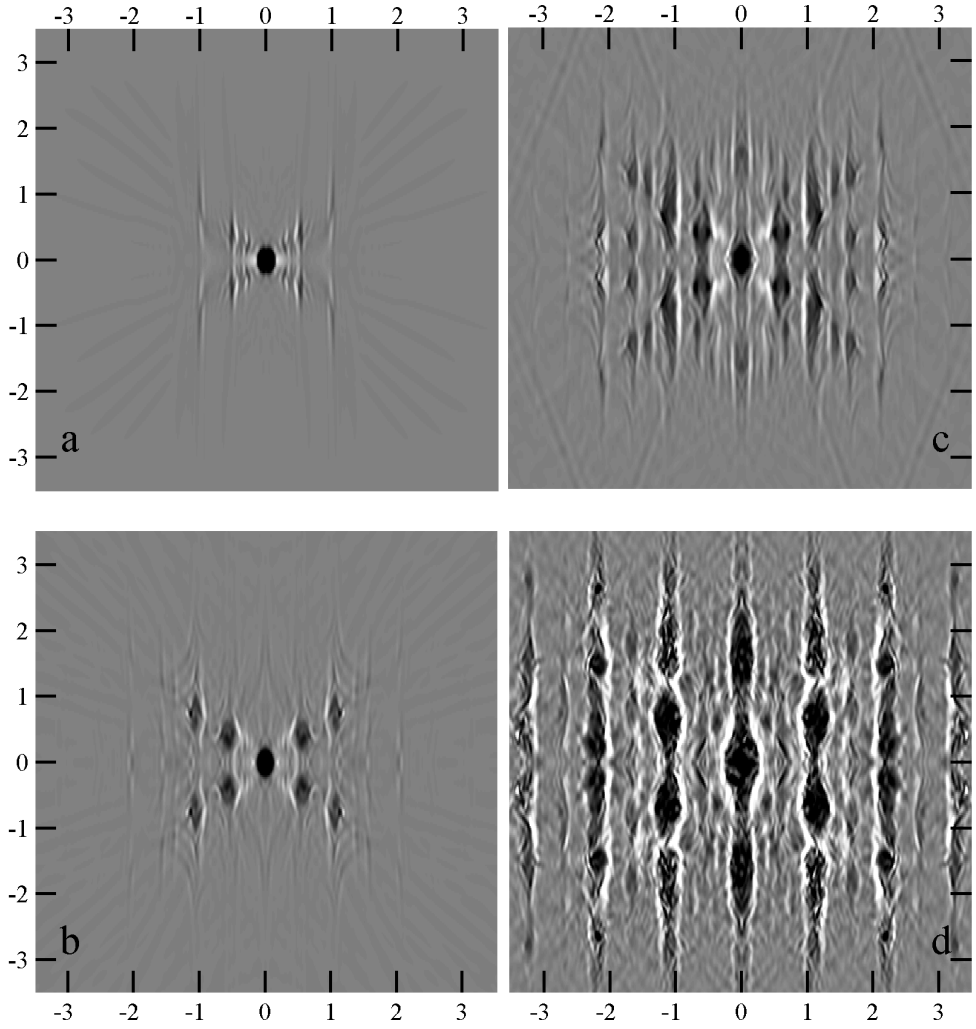

Figure 4.2: Zombie vortices sweep outward from the perturbing vortex at the origin in the x–z plane shown at $y = 0$ (the horizontal axis is x, the vertical axis is z). Anticyclonic ω_z is black and cyclonic is white. This is the same flow as in Figure 4.1. The computational domain has $|z| \leq 4.7124$ and is larger than shown. The Rossby number of the initial perturbing anticyclone at the origin is $Ro \equiv \omega_z/f = -0.31$. (a) $t = 128/N$. Only the vortex at the origin is present, but critical layers with $s = 0$ and $|m| = 1$, 2, and 3 are visible. The faint diagonal lines correspond to internal inertia-gravity waves with shear, not critical layers. (b) $t = 480/N$. 1^{st}-generation vortices near $|x| = 1$ and $1/2$ have rolled-up from critical layers with $s = 0$ and $|m| = 1$ and 2, respectively. (c) $t = 1632/N$. 2^{nd}-generation $|m| = 1$ vortices near $|x| = 0$ and 2 were spawned from the 1^{st} generation vortices near $|x| = 1$. Another 2^{nd}-generation of $|m| = 1$ vortices is near $|x| \simeq 1/2$ and $3/2$, which were spawned by the 1^{st} generation near $|x| = 1/2$. All 2^{nd}-generation vortices rolled up from critical layers with $|m| = 1$. (d) $t = 3072/N$. 1^{st}, 2^{nd} and 3^{rd} generation vortices.

where we assume periodic boundary conditions in z and y. When the density $\bar{\rho}$ is stably-stratified (i.e., with real $N \neq 0$) or constant ($N = 0$) this plane Couette flow is neutrally stable for all Ω (i.e., the imaginary part of s is zero and the eigenmodes neither grow nor decay). The eigen-equation for the stream functions of the eigenmodes of equations (4.5)–(4.7) is a generalization of Rayleigh's equation [Drazin and Reid, 2004] and is a 2^{nd}-order o.d.e. The coefficient of the highest-derivative term is

$$\left[\bar{V}(x) - \frac{s}{k_y}\right]\left[\left(\bar{V}(x) - \frac{s}{k_y}\right)^2 - \left(\frac{N}{k_y}\right)^2\right]. \tag{4.8}$$

It is well known that the eigenmodes of an o.d.e. are singular at locations x^* where the coefficient of the highest-derivative term of the eigen-equation is equal to zero. At x^*, the eigenmode has a *critical layer* [Drazin and Reid, 2004]. For fluids with constant density ($N \equiv 0$), the critical layers of uni-directional shearing flows have been well-studied and have $\bar{V}(x^*)$ equal to the phase speed s/k_y of the eigenmode. We refer to these as *barotropic critical layers*; they are not of interest to us because laboratory experiments and numerical calculations show that these critical layers are not easily excited and do not produce vortices. Eigenmodes with barotropic critical layers have singularities in the stream-wise components of their velocities, but not other components.

For $N \neq 0$, expression (4.8) shows that there are eigenmodes with barotropic critical layers at

$$\bar{V}(x^*) - s/k_y,$$

but we found that they remain difficult to excite and never form vortices. However, there is a new class of eigenmodes with critical layers with

$$\bar{V}(x^*) - s/k_y \pm N/k_y = 0.$$

We refer to the latter as *baroclinic critical layers*. These have not been explored before. Eigenmodes with baroclinic critical layers are neutrally stable (i.e., s is real). These eigenmodes are easily excited by small disturbances, always produce large-amplitude vortex layers, and often produce zombie vortices because their singularities are in the vertical z components of their velocities. To see why, note that the z-component of the curl of equation (4.5) gives

$$\frac{\partial \omega_z}{\partial t} = -(\mathbf{v}\cdot\nabla)\omega_z + (\omega\cdot\nabla)v_z + (f+\sigma)\frac{\partial v_z}{\partial z}, \tag{4.9}$$

where ω is the *relative* vorticity with respect to the equilibrium flow, i.e.,

$$\omega \equiv \nabla \times (\mathbf{v} - \bar{V}(x)\,\hat{\mathbf{y}}).$$

Equation (4.9) shows that the generalized Coriolis term

$$(f+\sigma)(\partial v_z/\partial z)$$

is a source for ω_z. Within the baroclinic critical layer, the z-component of the velocity is nearly anti-symmetric about the plane with $x = x^*$; on one side of the layer $v_z \to \infty$, and on the other side $v_z \to -\infty$; thus, the Coriolis term in equation (4.9) creates a large-magnitude vortex layer centered at x^* made of dipolar segments with one side having cyclonic vorticity ($\omega_z f > 0$) and the other with anticyclonic vorticity ($\omega_z f < 0$) (c.f., Figure 4.1a).

We consider only the case of anticyclonic shear with $\sigma < 0$ and $f > 0$. Note that PPDs have anticyclonic shear and are periodic in their stream-wise, or azimuthal, direction like the Couette flow studied here. The equations of motion (4.5)–(4.7) and boundary conditions are invariant under translations in y and z, and also under translation in x by δ when accompanied by a stream-wise boost in velocity of $\sigma\delta$. The latter symmetry is known as the *shift and boost symmetry*, c.f., [Goldreich and Lynden-Bell, 1965, Marcus and Press, 1977], and is exploited when using *shearing sheet* boundary conditions of PPDs [Barranco and Marcus, 2006, Balbus and Hawley, 1998]. From this point on, we use non-dimensional units with time in units of $1/N$ and length in units of

$$|(LN)/(2\pi\sigma)|,$$

where L is the periodicity length in the stream-wise direction, so k_y in expression (4.8) is $2\pi m/L$, where m is an integer. Baroclinic critical layers have $k_y \neq 0$, and expression (4.8) shows that in dimensionless units are at:

$$x^* = -\frac{s \pm 1}{m}. \tag{4.10}$$

Due to the shift-and-boost symmetry, the origin of the x-axis is not unique, so equation (4.10) has the following meaning: x^* is the cross-stream distance between a finite-amplitude perturbation and the location of the baroclinic critical layer that it excites.

4.3 Single Vortex Perturbation

Our numerical solutions of equations (4.5)–(4.7) show that many types of perturbations create zombie vortices. For verification, our solutions were computed with two independent codes using the methodology in [Barranco and Marcus, 2006]. One code treated the cross-stream boundaries as periodic with energy damping, and the other used the shearing sheet approximation. In the example in Figures 4.1 and 4.2, the initial perturbation is a small-volume anticyclone with a Rossby number

$$Ro \equiv \frac{\omega_z}{f}$$

of -0.31 at the origin superposed on the unperturbed flow $\bar{V}(x)$ and $\bar{\rho}(z)$. Figure 4.1 shows ω_z in an x–y plane. The perturbing vortex is steady, so it excites critical layers with temporal frequencies $s = 0$. Thus, equation (4.10) shows that the critical layers are at $|x^*| = 1/|m|$ and that the vortex at the origin has no critical layers with $x > 1$. At early times, Figure 4.1a

shows that vortex layers form at the critical layers: at each critical layer with wavenumber $|m|$, ω_z appears at $x = 1/|m|$ as $|m|$ segments of dipolar stripes aligned in the stream-wise y direction. A Fourier analysis shows that the stripes have $s = 0$. We have shown previously [Marcus, 1990, 1993] that in shear flows with $f\sigma < 0$, cyclonic vortex layers aligned in the stream-wise direction are stable, whereas anticyclonic layers are unstable, roll-up into discrete anticyclones, and merge to form one large anticyclone. This behavior is seen in Figure 4.1b. The anticyclonic vorticity at $x = 1/3$ has already rolled up and merged into a single large anticyclone (near $y = 1.5$). The anticyclonic vorticity at $x = 1/2$ has rolled up into a large anticyclone near $y = -0.5$. In contrast, the cyclonic ω_z near $x = 1/2$ has formed a continuous, but meandering, filament. At later times (Figure 4.1c) the anticyclones near $x = 1/3$ (and near $y = 2$) and near $x = 1/2$ (and near $y = -1$) have become larger. Moreover, Figures 4.1c and 4.1d show critical layers and vortices at $x > 1$, which cannot be created by the perturbation at the origin. The layers at $x > 1$ are due to the self-replication of the 1^{st}-generation vortices at $|x| \leq 1$. A vortex at *any* location will excite critical layers in a manner exactly like the original perturbing vortex at the origin due to the shift-and-boost symmetry (and will have $s = 0$ when viewed in the frame moving with the perturbing vortex). Figure 4.1c, shows 2^{nd}-generation critical layers at $x = 4/3$, $3/2$, 2, and $2/3$ all with $|m| = 1$ and excited by the 1^{st}-generation vortices at $x = 1/3$, $1/2$, 1, and $-1/3$, respectively. Figure 4.1d, shows 3^{rd}-generation critical layers at $2 < x \leq 3$, and 4^{th}-generation critical layers becoming excited at $x > 3$. At late times the vortices from $m = 1$ critical layers dominate the flow. (See Figure 4.2d.) At very late times, the vortices have widths in their cross-stream directions of order unity. (See below.)

Figure 4.2 shows the flow in Figure 4.1 viewed in the x–z plane and illustrates our main result: at late times the domain in the x–z plane fills with anticyclones. Because the flow is homogeneous with uniform σ and N, the vortices form a regular lattice despite the flow's turbulence. As time progresses in Figure 4.2, the vortex population spreads out from the perturbing vortex at the origin. At early times 4.2a) the flow has 1^{st}-generation critical layers, with $|m| = 1$, 2, and 3 being the most visible. In this first generation, and all subsequent generations, a perturbing vortex creates four vortices at its $|m| = 1$ critical layers. The new vortices form at locations in x that are $\pm l_x$ distant from the perturbing vortex and at locations in z that are $\pm l_z$ distant from the perturbing vortex. The distance in x between a perturbing vortex and the centerline of the $|m| = 1$ critical layer it excites (and the centerline of the dipolar vortex segment it creates) is unity, but the distance to the anticyclonic piece of the dipolar vortex is l_x, which is slightly greater than unity. At the time of Figure 4.2b the 2^{nd}-generation $m = 1$ critical layers created by the 1^{st}-generation vortices with $|m| = 1$, 2, and 3 are all visible near $|x| = 2l_x$, $(3/2)l_x$, and $(4/3)l_x$ respectively. At later times (Figure 4.2d), the $|m| = 1$ vortices that were descended from the 1^{st}-generation $|m| = 1$ vortices dominate the flow. These dominant vortices form a lattice and are located at

$$[x = 2n\ l_x, z = 2j\ l_z]$$

and at

$$[x = (2n+1)l_x, z = (2j+1)l_z],$$

for all integers n and j.

The characteristic $|Ro|$ of late-time zombie vortices is of order that of the initial perturbation. After a vortex forms, its $|Ro|$ intensifies to its approximate peak value within a few of its turn-around times, and it remains near that value indefinitely. Based on several numerical experiments, it appears that the late-time values of $|Ro|$ depend on the parameters, N, f and σ rather than on the properties of the initial perturbation. To examine the energy of the vortices and discover its source, we decomposed the flow's energy into two orthogonal parts: (1) the *zonal* component consisting of the kinetic energy of the stream-wise velocity component with Fourier modes $k_z = k_y = 0$ (i.e., the background shearing flow); and (2) the *non-zonal* component consisting of everything else, including the potential energy

$$g \int z(\rho - \bar{\rho}) \ (d\,\text{volume}).$$

If the initial flow were the unperturbed flow $\bar{V}(x)\hat{\mathbf{y}}$ and $\bar{\rho}$, then the initial energy would be all zonal. In the flow in Figures 4.1 and 4.2, there is a small initial non-zonal component of the energy due to the initial vortex at the origin. At late times, the non-zonal energy component represents the energy of the zombie vortices (and their turbulence and waves). After initial transients with faster than exponential growth, the non-zonal energy increases exponentially from just after the time of Figure 4.1a to the time in Figure 4.2d with an e-folding time of ~ 1000. The non-zonal energy component in Figure 4.2d is more than 400 times larger than its initial value, and that energy is supplied by the zonal component. The total energy is not conserved either with shearing sheet boundaries or with energy-damping periodic boundaries. In the latter, the vortices primarily lose energy by radiating internal, shearing inertia-gravity waves to the boundaries. If the self-replication is self-similar, we would expect the perimeter of the front between the vortex-dominated flow and unperturbed flow in each x-z plane to grow as t and the number of vortices to increase as t^2, which is consistent with our numerical experiments. After transients, the energy of the vortices, i.e., the non-zonal energy component, grows exponentially in time because the volume of each vortex grows exponentially in our calculations. That exponential growth must eventually stop because the cross-stream widths of the vortices cannot become larger than unity without them overlapping.

4.4 Conclusion

Neutrally-stable, shearing, stably-stratified Couette flow can be finite-amplitude unstable. In the example here, baroclinic critical layers are excited by a small vortex, but our calculations show that a variety of small-volume, small-energy perturbations cause critical layers to grow and roll-up into large-volume, large-energy vortices. In general, this instability self-replicates

with each new vortex exciting new layers that roll-up until the domain fills with compact 3D (i.e., not Taylor columns) vortices. The robustness of zombie vortices is self-evident from the fact that they are embedded in turbulent flows and survive indefinitely. They survive by drawing energy from the background shear flow at a rate that is faster than their dissipation rate. For constant N and σ, the unperturbed flow is homogeneous, and vortex self-replication is self-similar with zombie vortices forming a regular lattice. The regularity of the lattice allows for reinforcement: each vortex re-excites four other vortices in the lattice, and each vortex in the lattice is continually re-excited by four other vortices.

Zombie vortices occur frequently in our numerical simulations of Boussinesq and compressible fluids, so they pose a paradox: if they are so common, why have they not been reported earlier? We believe there are three reasons:

1. instabilities have not been systematically sought in stratified Couette flows [Le Bars and Le Gal, 2007];

2. with few exceptions [Tevzadze et al., 2008], stability studies of ideal gases in PPDs were carried out with no initial vertical stratification [Balbus et al., 1996, Shen et al., 2006];

3. the necessary spatial resolution to compute critical layers is lacking in many calculations.

Zombie vortices occur in our calculations of the dead zones of protoplanetary disks [Barranco and Marcus, 2005], which suggest that they may have an important role in star and planet formation. In addition, zombie vortices should be observable in laboratory circular Couette flows with stratified salt water for parameter values where the flow is linearly stable and where the angular momentum of the flow increases with increasing radius.

Appendix A

Suction Rate Function $q_O(\mathbf{x})$

As discussed in section 3.3, $q_o(\mathbf{x})$ is nearly uniform and negative inside a spherical region of radius R located at the center of the domain $\mathbf{x} = 0$. Outside the spherical region, q_o decays rapidly. Therefore, the profile of q_o in each direction looks like a top–hat function of width $2R$ with smoothed edges.

In a triply periodic domain, the integral of $q_o(\mathbf{x})$ over the entire domain must be zero. This is because, integrating (3.7) over the entire domain gives

$$\underbrace{\int \frac{\partial u}{\partial x} d\mathbf{x}}_{=0} + \underbrace{\int \frac{\partial v}{\partial y} d\mathbf{x}}_{=0} + \underbrace{\int \frac{\partial w}{\partial z} d\mathbf{x}}_{=0} = \int q_o(\mathbf{x}) d\mathbf{x} \tag{A.1}$$

where each term on the left–hand side is found to be zero using the divergence theorem and periodicity (the time dependence of q is ignored for simplicity). The integral of $q_o(\mathbf{x})$ over the spherical suction region (i.e., sink) is equal to $Q_o < 0$. Therefore, to satisfy the requirement in (A.1), an injection region (i.e., source) must exist in the domain. In another word, this is because the sucked flow cannot be supplied through periodic boundaries.

Here we have chosen to evenly spread the source over the entire space outside the spherical sink. Therefore, the integral of $q_o(\mathbf{x})$ over the region outside the spherical suction region is $-Q_o > 0$. Because the volume of a sphere with radius R is much smaller than the volume of the entire domain with width $D = 20R$, the distributed injection $q_o > 0$ (outside the sphere) is much weaker than the localized suction $q_o < 0$ (inside the sphere). As a result, this choice of source is not expected to significantly affect the flow field. Particularly, we remind the reader that because of the third term on the right–hand side of (3.10), the (small) amount of fluid injected into the domain at each point has the same momentum as the local momentum of the flow. Excluding this term would have resulted in injecting fluid with zero velocity into a point that might have non-zero local velocity, resulting in a fictitious drag. Such drag can be significant in a strongly rotating flow where velocities are large even far from the sink because of the (background) solid–body rotation.

Note that unlike Davey and Killworth [1989], McDonald [1992] and us, Aiki and Yamagata [2000, 2004] did not include the equivalent of the $\rho q \mathbf{v}$ term on the right–hand side of

(3.10) in their shallow–water equations. Therefore, the $\rho q \mathbf{v}$ term arising from the $\nabla \cdot (\rho \mathbf{v}\mathbf{v})$ term on the left hand–side of (3.10) is not canceled out in the formulation presented by Aiki and Yamagata [2000] (their equation (2.3)). However, these authors did not include the contribution of the solid–body rotation to the velocity field of the shallow–water equivalent of the uncanceled $\rho q \mathbf{v}$ term, resulting in this term (in the rotating frame) being small compared to the Coriolis term. As a result, Aiki and Yamagata [2000] found their results to be insensitive to the existence of this term, and not significantly different from the results reported by Davey and Killworth [1989].

Bibliography

M. A. Abramowicz, A. Lanza, E. A. Spiegel, and E. Szuszkiewicz. Vortices on accretion disks. *Nature*, 356(6364):41–43, 1992.

H. Aiki and T. Yamagata. Successive formation of planetary lenses in an intermediate layer. *Geophysical & Astrophysical Fluid Dynamics*, 92(1-2):1–29, 2000.

H. Aiki and T. Yamagata. A numerical study on the successive formation of Meddy-like lenses. *Journal of Geophysical Research: Oceans*, 109, 2004.

L. Armi, D. Hebert, N. Oakey, J. F. Price, P. L. Richardson, H. T. Rossby, and B. Ruddick. The history and decay of a Mediterranean salt lens. *Nature*, 333(6174):649–651, 1988.

L. Armi, D. Hebert, N. Oakey, J. F. Price, P. L. Richardson, H. T. Rossby, and B. Ruddick. Two years in the life of a Mediterranean salt lens. *Journal of Physical Oceanography*, 19 (3):354–370, 1989.

P. J. Armitage. Dynamics of protoplanetary disks. *Annual Review of Astronomy and Astrophysics*, 49:195–236, 2011.

O. Aubert, M. Le Bars, P. Le Gal, and P. S. Marcus. The universal aspect ratio of vortices in rotating stratified flows: experiments and observations. *Journal of Fluid Mechanics*, 706:34, 2012.

S. A. Balbus and J. F. Hawley. Instability, turbulence, and enhanced transport in accretion disks. *Reviews of Modern Physics*, 70(1), 1998.

S. A. Balbus, J. F. Hawley, and J. M. Stone. Nonlinear stability, hydrodynamical turbulence, and transport in disks. *The Astrophysical Journal*, 467, 1996.

V. Barcilon and J. Pedlosky. On the steady motions produced by a stable stratification in a rapidly rotating fluid. *Journal of Fluid Mechanics*, 29:673–690, 1967.

P. Barge and J. Sommeria. Did planet formation begin inside persistent gaseous vortices. *Astronomy and Astrophysics*, 295(1):L1–L4, 1995.

J. A. Barranco and P. S. Marcus. Three-dimensional vortices in stratified protoplanetary disks. *Astrophysical Journal*, 623(2):1157–1170, 2005.

J. A. Barranco and P. S. Marcus. A 3D spectral anelastic hydrodynamic code for shearing, stratified flows. *Journal of Computational Physics*, 219(1):21–46, 2006.

P. Billant and J-M Chomaz. Self-similarity of strongly stratified inviscid flows. *Physics of Fluids*, 13(6):1645–1651, 2001.

N. Boulanger, P. Meunier, and S. Le Dizès. Structure of a stratified tilted vortex. *Journal of Fluid Mechanics*, 583(1):443–458, 2007.

A. Bracco, P. H. Chavanis, A. Provenzale, and E. A. Spiegel. Particle aggregation in a turbulent Keplerian flow. *Physics of Fluids*, 11:2280, 1999.

J. W. M. Bush and A. W. Woods. Vortex generation by line plumes in a rotating stratified fluid. *Journal of Fluid Mechanics*, 388:289–313, 1999.

X. Carton. Hydrodynamical modeling of oceanic vortices. *Surveys in Geophysics*, 22(3): 79–263, 2001.

C. Cenedese and P. F. Linden. Cyclone and anticyclone formation in a rotating stratified fluid over a sloping bottom. *Journal of Fluid Mechanics*, 381:199–223, 1999.

J. G. Charney. Geostrophic turbulence. *Journal of the Atmospheric Sciences*, 28:1087–1095, 1971.

J. Y. K. Cho and L. M. Polvani. The emergence of jets and vortices in freely evolving, shallow–water turbulence on a sphere. *Physics of Fluids*, 8(6):1531–1552, 1996a.

J. Y-K. Cho and L. M. Polvani. The morphogenesis of bands and zonal winds in the atmospheres on the giant outer planets. *Science*, pages 335–336, 1996b.

S. B. Dalziel, G. O. Hughes, and B. R. Sutherland. Whole-field density measurements by synthetic schlieren. *Experiments in Fluids*, 28(4):322–335, 2000.

M. K. Davey and P. D. Killworth. Flows produced by discrete sources of buoyancy. *Journal of Physical Oceanography*, 19:1279–1290, 1989.

I. de Pater, M. H. Wong, P. S. Marcus, S. Luszcz-Cook, M. Ádámkovics, A. Conrad, X. Asay-Davis, and C. Go. Persistent rings in and around Jupiter's anticyclones–observations and theory. *Icarus*, 210(2):742–762, 2010.

P. G. Drazin and W. H. Reid. *Hydrodynamic stability*. Cambridge University Press, 2004.

D. G. Dritschel, M. D. Juarez, and M. H. P. Ambaum. The three-dimensional vortical nature of atmospheric and oceanic turbulent flows. *Physics of Fluids*, 11(6):1512–1520, 1999.

L. N Fletcher et al. Thermal structure and composition of Jupiters Great Red Spot from high-resolution thermal imaging. *Icarus*, 208(1):306–328, 2010.

P. R. Gent and J. C. McWilliams. The instability of barotropic circular vortices. *Geophysical and Astrophysical Fluid Dynamics*, 35:209–233, 1986.

M. Ghil, M. D. Chekroun, and E. Simonnet. Climate dynamics and fluid mechanics: Natural variability and related uncertainties. *Physica D: Nonlinear Phenomena*, 237(14):2111–2126, 2008.

A. E. Gill. Homogeneous intrusions in a rotating stratified fluid. *Journal of Fluid Mechanics*, 103:275–295, 1981.

C. Y. Go, I. de Pater, M. Wong, S. Lockwood, P. S. Marcus, X. Asay-Davis, and S. Shetty. Evolution of the Oval BA during 2004–2005. In *Bulletin of the American Astronomical Society*, volume 38, page 495, 2006.

D. A. Godfrey. A hexagonal feature around Saturn's North Pole. *Icarus*, 76(2):335–356, 1988.

P. Goldreich and D. Lynden-Bell. Ii. spiral arms as sheared gravitational instabilities. *Monthly Notices of the Royal Astronomical Society*, 130:125, 1965.

L. P. Graves, J. C. McWilliams, and M. T. Montgomery. Vortex evolution due to straining: a mechanism for dominance of strong, interior anticyclones. *Geophysical & Astrophysical Fluid Dynamics*, 100(3):151–183, June 2006.

H. P. Greenspan. *The theory of rotating fluids*. Cambridge University Press, 1990.

R. W. Griffiths and P. F. Linden. The stability of vortices in a rotating, stratified fluid. *Journal of Fluid Mechanics*, 105:283–316, 1981.

G. J. Hakim, C. Snyder, and D. J. Muraki. A new surface model for cyclone–anticyclone asymmetry. *Journal of the Atmospheric Sciences*, 59(16):2405–2420, 2002.

P. Hassanzadeh and P. S. Marcus. 3d baroclinic vortices in rotating stratified shear: from an orange great red spot to planet formation. In *Bulletin of the American Physical Society*, volume 57. APS, 2012.

P. Hassanzadeh, P. S. Marcus, and P. Le Gal. The universal aspect ratio of vortices in rotating stratified flows: theory and simulation. *Journal of Fluid Mechanics*, 706:46, 2012.

P. Hassanzadeh, O. Aubert, P. S. Marcus, M. Le Bars, and P. Le Gal. Three–dimensional cyclones produced by localised suction in rotating stratified flows: a numerical and experimental study. *to be submitted to the Journal of Fluid Mechanics*, 2013.

H. J. Head. *The use of miniature four-electrode conductivity probes for high-resolution measurements of turbulent density or temperature variations in salt-stratified water flows*. PhD thesis, University of California, San Diego, 1983.

K. Hedstrom and L. Armi. An experimental-study of homogeneous lenses in a stratified rotating fluid. *Journal of Fluid Mechanics*, 191:535–556, 1988.

A. J. Hines, A.and Willmott. Unsteady abyssal circulation driven by a discrete buoyancy source in a continuously stratified ocean. *Journal of Physical Oceanography*, 27(7):1349–1370, 1997.

R. Hooke. A spot in one of the belts of Jupiter. *Philosophical Transactions*, 1, 1665.

T. Humphreys and P. S. Marcus. Vortex street dynamics: The selection mechanism for the areas and locations of Jupiter's vortices. *Journal of the Atmospheric Sciences*, 64(4): 1318–1333, 2007.

A. P. Ingersoll. Atmospheric dynamics of the outer planets. *Science*, 248(4953):308–315, 1990.

A. P. Ingersoll and P. G. Cuong. Numerical model of long–lived Jovian vortices. *Journal of the Atmospheric Sciences*, 38(10):2067–2076, 1981.

A. Jenkins. An elementary treatment of the reverse sprinkler. *American Journal of Physics*, 72(10):1276–1283, 2004.

H. Ji, M. Burin, E. Schartman, and J. Goodman. Hydrodynamic turbulence cannot transport angular momentum effectively in astrophysical disks. *Nature*, 444(7117):343–346, 2006.

B. Khouider, A. J. Majda, and S. N. Stechmann. Climate science in the tropics: waves, vortices and PDEs. *Nonlinearity*, 26(1):R1, 2013.

H. Klahr and P. Bodenheimer. Formation of giant planets by concurrent accretion of solids and gas inside an anticyclonic vortex. *The Astrophysical Journal*, 639(1):432, 2006.

P. Klein and G. Lapeyre. The oceanic vertical pump induced by mesoscale and submesoscale turbulence. *Annual Review of Marine Science*, 1:351–375, 2009.

I. Koszalka, A. Bracco, J. C. McWilliams, and A. Provenzale. Dynamics of wind–forced coherent anticyclones in the open ocean. *Journal of Geophysical Research*, 114, 2009.

P. K. Kundu and I. M. Cohen. *Fluid Mechanics*. Academic Press, 2010.

M. Le Bars and P. Le Gal. Experimental analysis of the stratorotational instability in a cylindrical Couette flow. *Physical Review Letters*, 99(6), 2007.

P. F. Linden, B. M. Boubnov, and S. B. Dalziel. Source–sink turbulence in a rotating stratified fluid. *Journal of Fluid Mechanics*, 298(1):81–112, 1995.

J. J. Lissauer. Planet formation. *Annual Review of Astronomy and Astrophysics*, 31:129–174, 1993.

R. V. E. Lovelace, H. Li, S. A. Colgate, and A. F. Nelson. Rossby wave instability of Keplerian accretion disks. *The Astrophysical Journal*, 513(2), 1999.

W. Lyra and M-M Mac Low. Rossby wave instability at Dead Zone boundaries in three–dimensional resistive magnetohydrodynamical global models of protoplanetary disks. *The Astrophysical Journal*, 756(1):62, 2012.

M-M Mac Low and A. P. Ingersoll. Merging of vortices in the atmosphere of Jupiter: An analysis of Voyager images. *Icarus*, 65(2):353–369, 1986.

P. S. Marcus. Numerical-simulation of Jupiter's Great Red Spot. *Nature*, 331(6158):693–696, 1988.

P. S. Marcus. Vortex dynamics in a shearing zonal flow. *Journal of Fluid Mechanics*, 215: 393–430, 1990.

P. S. Marcus. Jupiter's Great Red Spot and other vortices. *Annual Review of Astronomy and Astrophysics*, 31:523–573, 1993.

P. S. Marcus. Prediction of a global climate change on Jupiter. *Nature*, 428(6985):828–831, 2004.

P. S. Marcus and P. Hassanzadeh. 3D vortices in stratified, rotating flows-secondary circulations and changes in aspect radio due to dissipation. In *Bulletin of the American Physical Society*, volume 56. APS, 2011.

P. S. Marcus and W. H. Press. On Green's functions for small disturbances of plane Couette flow. *Journal of Fluid Mechanics*, 79(03):525–534, 1977.

P. S. Marcus, X. S. Asay-Davis, M. H. Wong, and I. de Pater. Jupiters Red Oval BA: Dynamics, color, and relationship to Jovian climate change. *Journal of Heat Transfer*, 135, 2013a.

P. S. Marcus, S. Pei, C-H Jiang, and P. Hassanzadeh. Self–replicating three–dimensional vortices in neutrally–stable stratified rotating shear flows. *submitted to the Physical Review Letters*, 2013b.

N. R. McDonald. Flows caused by mass forcing in a stratified ocean. *Deep Sea Research A*, 39(10):1767–1790, 1992.

M. E. McIntyre. On the antarctic ozone hole. *Journal of Atmospheric and Terrestrial Physics*, 51(1):29–43, 1989.

M. E. McIntyre. The stratospheric polar vortex and sub-vortex: Fluid dynamics and midlatitude ozone loss. *Philosophical Transactions of the Royal Society of London A*, 352(1699): 227–240, 1995.

C. F. McKee and E. C. Ostriker. Theory of star formation. *Annual Review of Astronomy and Astrophysics*, 45(1):565–687, 2007.

J. C. McWilliams. Submesoscale, coherent vortices in the ocean. *Reviews of Geophysics*, 23 (2):165–182, 1985.

J. C. McWilliams. Vortex generation through balanced adjustment. *Journal of Physical Oceanography*, 18(8):1178–1192, 1988.

J. C. McWilliams, J. B. Weiss, and I. Yavneh. Anisotropy and coherent vortex structures in planetary turbulence. *Science*, 264(5157):410–413, 1994.

J. C. McWilliams, J. B. Weiss, and I. Yavneh. The vortices of homogeneous geostrophic turbulence. *Journal of Fluid Mechanics*, 401:1–26, 1999.

F. Moisy, C. Morize, M. Rabaud, and J. Sommeria. Decay laws, anisotropy and cyclone–anticyclone asymmetry in decaying rotating turbulence. *Journal of Fluid Mechanics*, 666: 5–35, October 2010.

R. Morales-Juberías and T. E. Dowling. Jupiters Great Red Spot: Fine–scale matches of model vorticity patterns to prevailing cloud patterns. *Icarus*, 2013.

Y. Morel and J. McWilliams. Evolution of isolated interior vortices in the ocean. *Journal of Physical Oceanography*, 27(5):727–748, 1997.

D. Nof. On the β-induced movement of isolated baroclinic eddies. *Journal of Physical Oceanography*, 11(12):1662–1672, 1981.

D. B. Olson. Rings in the ocean. *Annual Review of Earth and Planetary Sciences*, 19:283, 1991.

M. S. Paoletti, D. P. M. van Gils, B. Dubrulle, C. Sun, D. Lohse, and D. P. Lathrop. Angular momentum transport and turbulence in laboratory models of Keplerian flows. *Astronomy & Astrophysics*, 547, 2012.

J. Pedlosky. *Geophysical fluid dynamics*. Springer–Verlag, 1990.

G. Perret, A. Stegner, M. Farge, and T. Pichon. Cyclone–anticyclone asymmetry of large–scale wakes in the laboratory. *Physics of Fluids*, 18, 2006.

G. Perret, T. Dubos, and A. Stegner. How large–scale and cyclogeostrophic barotropic instabilities favor the formation of anticyclonic vortices in the ocean. *Journal of Physical Oceanography*, 41(2):303–328, 2011.

L. M. Polvani, J. C. McWilliams, M. A. Spall, and R. Ford. The coherent structures of shallow–water turbulence: Deformation–radius effects, cyclone/anticyclone asymmetry and gravity–wave generation. *Chaos: An Interdisciplinary Journal of Nonlinear Science*, 4(2):177–186, 1994.

O. Praud, J. Sommeria, and A. M. Fincham. Decaying grid turbulence in a rotating stratified fluid. *Journal of Fluid Mechanics*, 547:389–412, 2006.

Lord Rayleigh. On the dynamics of revolving fluids. *Proceedings of the Royal Society of London. Series A*, 93(648):148–154, 1917.

J. N. Reinaud, D. G. Dritschel, and C. R. Koudella. The shape of vortices in quasi-geostrophic turbulence. *Journal of Fluid Mechanics*, 474:175–192, 2003.

C-G Rossby. A mechanism for the release of potential energy in the atmosphere. *Journal of Atmospheric Sciences*, 6:164–180, 1949.

G. Roullet and P. Klein. Cyclone–anticyclone asymmetry in geophysical turbulence. *Physical Review Letters*, 104(21):28–31, 2010.

C. Salyk, A. P. Ingersoll, J. Lorre, A. Vasavada, and A. D. Del Genio. Interaction between eddies and mean flow in Jupiter's atmosphere: Analysis of Cassini imaging data. *Icarus*, 185(2):430–442, 2006.

A. Sánchez-Lavega, R. Hueso, S. Pérez-Hoyos, and J. F. Rojas. A strong vortex in Saturn's South Pole. *Icarus*, 184(2):524–531, 2006.

P. Sangrà et al. The Canary eddy corridor: A major pathway for long–lived eddies in the subtropical North Atlantic. *Deep–Sea Research I*, 56(12):2100–2114, 2009.

K. M. Sayanagi, P. Morales-Juberias, and A. P. Ingersoll. Saturn's Northern Hemisphere Ribbon: Simulations and comparison with the meandering Gulf Stream. *Journal of the Atmospheric Sciences*, 67(8):2658–2678, 2010.

Y. Shen, J. M. Stone, and T. A. Gardiner. Three-dimensional compressible hydrodynamic simulations of vortices in disks. *The Astrophysical Journal*, 653(1), 2006.

S. Shetty and P. S. Marcus. Changes in Jupiter's Great Red Spot (1979-2006) and Oval BA (2000-2006). *Icarus*, 210(1):182–2018, 2010.

S. Shetty, X. S. Asay-Davis, and P. S. Marcus. On the interaction of Jupiter's Great Red Spot and zonal jet streams. *Journal of the Atmospheric Sciences*, 64, 2007.

A. Siegel, J. B. Weiss, J. Toomre, J. C. McWilliams, P. S. Berloff, and I. Yavneh. Eddies and vortices in ocean basin dynamics. *Geophysical Research Letters*, 28(16):3183–3186, 2001.

B. A. Smith et al. Voyager 2 at Neptune: Imaging science results. *Science*, 246(4936), 1989.

W. D. Smyth and J. C. McWilliams. Instability of an axisymmetric vortex in a stably stratified, rotating environment. *Theoretical and Computational Fluid Dynamics*, 11(3): 305–322, 1998.

J. Sommeria, S. D. Meyers, and H. L. Swinney. Laboratory simulation of Jupiters great red spot. *Nature*, 331(6158):689–693, 1988.

A. Stegner and D. G. Dritschel. A Numerical Investigation of the Stability of Isolated Shallow Water Vortices. *Journal of Physical Oceanography*, 30(10):2562–2573, October 2000.

G. A. Stuart, M. A. Sundermeyer, and D. Hebert. On the geostrophic adjustment of an isolated lens: Dependence on burger number and initial geometry. *Journal of Physical Oceanography*, 41(4):725–741, 2011.

A. G. Tevzadze, G. D. Chagelishvili, and J. P. Zahn. Hydrodynamic stability and mode coupling in Keplerian flows: local strato-rotational analysis. *Astronomy and Astrophysics*, 478(1):9–15, 2008.

G. K. Vallis. *Atmospheric and Oceanic Fluid Dynamics*. Cambridge University Press, 2006.

G. J. F. van Heijst and H. J. H. Clercx. Laboratory Modeling of Geophysical Vortices. *Annual Review of Fluid Mechanics*, 41:143–164, 2009.

G. J. F. van Heijst and R. C. Kloosterziel. Tripolar vortices in a rotating fluid. *Nature*, 338 (6216):569–571, 1989.

A. R. Vasavada and A. P. Showman. Jovian atmospheric dynamics: An update after Galileo and Cassini. *Reports on Progress in Physics*, 68(8):1935–1996, 2005.

H. von Zeipel. The radiative equilibrium of a rotating system of gaseous masses. *Monthly Notices of the Royal Astronomical Society*, 84:665–683, 1924.

D. W. Waugh and L. M. Polvani. Stratospheric polar vortices. *The Stratosphere: Dynamics, Transport, and Chemistry, Geophysics Monograph Series*, 190:43–57, 2010.

M. H. Wong, I. de Pater, X. Asay-Davis, P. S. Marcus, and C. Y. Go. Vertical structure of Jupiters Oval BA before and after it reddened: What changed? *Icarus*, 215(1):211–225, 2011.

W. Zenk and L. Armi. The complex spreading pattern of Mediterranean water off the Portuguese continental slope. *Deep–Sea Research*, 37(12):1805–1823, 1990.